Suzaku Results on Cygnus X-1 in the Low/Hard State

Kazuo MAKISHIMA,[1,2] Hiromitsu TAKAHASHI,[3] Shin'ya YAMADA,[1] Chris DONE,[4] Aya KUBOTA,[5] Tadayasu DOTANI,[6]
Ken EBISAWA,[6] Takeshi ITOH,[1] Shunji KITAMOTO,[7] Hitoshi NEGORO,[8] Yoshihiro UEDA,[9] and Kazutaka YAMAOKA[10]

[1] *Department of Physics, The University of Tokyo, 7-3-1 Hongo, Bunkyo-ku, Tokyo 113-0033*
maxima@phys.s.u-tokyo.ac.jp

[2] *Cosmic Radiation Laboratory, Institute of Physical and Chemical Research (RIKEN),*
2-1 Hirosawa, Wako-shi, Saitama 351-0198

[3] *Department of Physical Science, School of Science, Hiroshima University,*
1-3-1 Kagamiyama, Higashi-Hiroshima, Hiroshima 739-8526

[4] *Department of Physics, Durham University, South Road, Durham, DH1 3LE, UK*

[5] *Department of Electronic Information Systems, Shibaura Institute of Technology,*
307 Fukasaku, Minuma-ku, Saitama-shi, Saitama 337-8570

[6] *Institute of Space and Astronautical Science, JAXA, 3-1-1 Yoshinodai, Sagamihara, Kanagawa 229-8510*

[7] *Department of Physics, Rikkyo University, 3-34-1 Nishi-Ikebukuro, Toshima-ku, Tokyo 171-8501*

[8] *Department of Physics, College of Science and Technology, Nihon University, 1-8 Kanda-Surugadai, Chiyoda-ku, Tokyo 101-8308*

[9] *Department of Astronomy, Kyoto University, Kitashirakawa-Oiwake-cho, Sakyo-ku, Kyoto 606-8502*

[10] *Department of Physics & Mathematics, Aoyama Gakuin University, 5-10-1 Sagamihara, Kanagawa 229-8558*

Abstract

The black-hole binary Cygnus X-1 was observed for 17 ks with the Suzaku X-ray observatory in 2005 October, while it was in a low/hard state with a 0.7–300 keV luminosity of 4.6×10^{37} erg s^{-1}. The XIS and HXD spectra, spanning 0.7–400 keV, were reproduced successfully, incorporating a cool accretion disk and a hot Comptonizing corona. The corona is characterized by an electron temperature of ~ 100 keV, and two optical depths of ~ 0.4 and ~ 1.5, which account for the softer and harder continua, respectively. The disk has an innermost temperature of ~ 0.2 keV, and is thought to protrude half way into the corona. The disk not only provides seed photons to the Compton cloud, but also produces a soft spectral excess, a mild reflection hump, and a weakly broadened iron line. A comparison with the Suzaku data on GRO J1655$-$40 reveals several interesting spectral differences, which can mostly be attributed to inclination effects, assuming that the disk has a flat geometry while the corona is grossly spherical. An intensity-sorted spectroscopy indicates that the continuum becomes less Comptonized when the source flares up on time scales of 1–200 s, while the underlying disk remains unchanged.

Key words: accretion disks — black hole physics — stars: individual (Cygnus X-1) — X-ray: binaries

1. Introduction

Luminous soft X-ray radiation of accreting stellar-mass black holes (BHs) has generally been explained as thermal emission from optically thick (in particular "standard") accretion disks (Shakura & Sunyaev 1973; Makishima et al. 1986; Dotani et al. 1997; Remillard & McClintock 2006), which are expected to form around them under rather high accretion rates. In contrast, their hard X-ray production process is much less understood, even though intense hard X-ray emission characterizes black-hole binaries (BHBs) among various types of compact X-ray sources in the Milky Way and Magellanic clouds.

Indeed, BHBs often emit a major fraction of their radiative luminosity in the hard X-ray band, in the form of a spectral hard-tail component if they are in a so-called high/soft state, or as the entire power-law (hereafter PL) like continua if they are in a so-called low/hard state (hereafter LHS) which appears under relatively low accretion rates. Furthermore, the hard X-ray emission (particularly in the LHS) involves another interesting aspect, namely a long-known aperiodic variation

over a wide frequency range (e.g., Oda et al. 1971; Oda 1977; Nolan et al. 1981, Miyamoto et al. 1992; Pottschmidt et al. 2003; Remillard & McClintock 2006). These spectral and timing studies are not limited to stellar-mass BHs, since a fair fraction of active galactic nuclei (AGNs) are also considered to be in a state analogous to the LHS of BHBs, emitting luminous hard X-rays (e.g., Mushotzky et al. 1993).

In hard X-rays, a BHB in the LHS emits a roughly PL-shaped continuum with a photon index of $\Gamma \sim 1.7$ (e.g., Remillard & McClintock 2006), but the spectrum gradually steepens toward higher energies. This has been explained in terms of unsaturated Comptonization of some soft seed photons, in a cloud of hot Maxwellian electrons, or a "corona", with a temperature of $T_{\rm e} = 50$–100 keV and an optical depth of $\tau \sim 1$ (Shapiro et al. 1976; Sunyaev & Trümper 1979; Sunyaev & Titarchuk 1980; Gierliński et al. 1997; Di Salvo et al. 2001; Frontera et al. 2001a; Zdziarski & Gierliński 2004; Ibragimov et al. 2005). As a result, the Comtpon y-parameter, $y \equiv 4\tau k T_{\rm e}/(m_{\rm e} c^2)$, also takes a value of ~ 1, where k is the Boltzmann constant, $m_{\rm e}$ is the electron mass, and c is the light velocity. The electrons will be cooled by transferring

their energies to photons, while being heated via Coulombic collisions by ions that acquire nearly a free-fall temperature (e.g., Zdziarski et al. 1999). The Comptonizing cloud may be identified with radiatively inefficient inner accretion flow (e.g., Ichimaru 1977; Narayan & Yi 1995).

Superposed on the dominant continuum characterizing the LHS, we often observe a spectral hump at energies of 20–40 keV due to "reflection" of the primary X-rays by some cool materials (e.g., Lightman & White 1988; Inoue 1989), a fluorescent Fe-K emission line (Basko 1978; Kitamoto et al. 1990), and an apparently "smeared" Fe-K edge (Ebisawa et al. 1994). These features can be explained by assuming that a fraction of the primary hard X-rays are reprocessed by cool materials located near the BH, presumably an optically-thick part of the accretion disk (Done et al. 1992; Marshall et al. 1993; Ebisawa et al. 1996, Gierliński et al. 1997). This part of the disk may at the same time produce an X-ray excess that we often observe at the softest end of the spectrum (e.g., Bałucińska & Hasinger 1991), and furthermore, may provide the Comptonizing corona with the seed photons (e.g., Shapiro et al. 1976).

In spite of the general success of this currently popular interpretation of the LHS in terms of Comptonizing hot clouds and cool materials, details of the scenario still need to be elucidated. It is yet to be confirmed that the seed photons are provided by a cool accretion disk (e.g., Zdziarski et al. 1999), rather than by thermal cyclotron emission in the Compton corona, itself (e.g., Kanbach et al. 2001). The geometry and size of the Comptonizing cloud is not well known, except for loose constraints, including; that the cloud should be large enough for the compactness parameter to remain within a reasonable range (Lightman & Zdziarski 1987), but should not be too large to be able to produce the hard X-ray variation on a ~ 1 s time scale, and that it should have a sufficient vertical height so as to efficiently illuminate the reprocessing matter. Still unsettled is the relation between the hot corona and the putative cool disk; whether the cool disk is truncated at a large radius (Zdziarski et al. 1998; Done & Życki 1999; Zdziarski et al. 2004), or it penetrates deep into the hot corona (Young et al. 2001; Miller et al. 2006a). Yet another fundamental issue is how to understand the violent hard X-ray variability in the context of thermal Comptonization scenario (e.g., Miyamoto et al. 1988).

To address these issues associated with the LHS of accreting BHs, a number of spectral studies have been conducted so far, by fitting observed broad-band spectra with theoretical spectral models (e.g., Gierliński et al. 1997; Zdziarski et al. 1998; Dove et al. 1998; Frontera et al. 2001a). Similarly, extensive studies in the frequency domain have been conducted to characterize the random variations (e.g., Miyamoto & Kitamoto 1989; Negoro et al. 1994; Nowak et al. 1999a; Gilfanov et al. 2000; Revnivtsev et al. 2000; Remillard & McClintock 2006). However, the former approach is limited in that different modelings often degenerate. The latter approach also has a limitation, in that it may not constrain details of the Comptonization scenario without invoking particular models (Kazanas et al. 1997; Hua et al. 1997).

We analyze broad-band (0.7–400 keV) Suzaku data of Cygnus X-1 (Cyg X-1: Oda 1977; Liang & Nolan 1984) acquired in 2005 October. With the wide-band sensitivity,

Suzaku is expected to provide novel diagnostics of this BHB, the first celestial object suspected to be a black hole (Oda et al. 1971). To overcome the above difficulties, we compare the Suzaku spectra of Cyg X-1 with those of GRO J1655−40, searching the two spectra for differences attributable to their different system inclination, $i \sim 45°$ of Cyg X-1 (Abubekerov et al. 2004) and $i \sim 70°$ of GRO J1655−40 (Greene et al. 2001). We hence refer to the Suzaku results on GRO J1655−40 by Takahashi et al. (2008) as Paper I. We also analyze spectral changes associated with the random variations on a time scale of ~ 1 s (section 4), to see how the Compton parameters are changing; this will be complementary to the study of long-term spectral changes (e.g., Ibragimov et al. 2005). We employ a distance of 2.5 kpc (Margon et al. 1973; Bregman et al. 1973) to Cyg X-1. The errors refer to statistical 90% confidence limits.

2. Observation and Data Processing

2.1. Observation

The present Suzaku observation of Cyg X-1 was performed on 2005 October 5, from UT 04:34 through 15:11 for a net exposure of 17.4 ks, as a part of the initial performance verification program of Suzaku (Mitsuda et al. 2007). Suzaku carries 4 sets of X-ray telescopes (Serlemitsos et al. 2007), each coupled to a focal-plane X-ray CCD camera called XIS (X-ray Imaging Spectrometer: Koyama et al. 2007) operating in the energy range of 0.2–12 keV. Three (XIS 0, XIS 2, and XIS 3) of the four XIS sensors use front-illuminated (FI) CCDs, while XIS 1 utilizes a back-illuminated (BI) one, thus achieving an improved soft X-ray response. The Hard X-ray Detector (HXD: Takahashi et al. 2007; Kokubun et al. 2007) covers the 10–70 keV energy band with Si PIN photo-diodes (HXD-PIN), and the 50–600 keV range with GSO scintillation counters (HXD-GSO).

Because the optical axes of the XIS and the HXD are slightly ($\sim 3'.5$) offset, the observation was carried out with the source placed at the center of the XIS field of view. The HXD was operated in the nominal mode throughout the observation. Because the source was very bright, the XIS was operated with the "1/8 window option", in which a smaller field of view of $17'.8 \times 2'.2$ is read out every 1 s. The editing mode of the FI CCDs was set to 2×2, while that of the BI CCD (XIS 1) was 3×3. In the present observation, however, XIS 1 with the BI CCD chip suffered severe telemetry saturation, for more than 60% of the total exposure.

During the observation, the averaged source count rates (excluding backgrounds) of XIS 0, HXD-PIN, and HXD-GSO were ~ 300, ~ 47, and ~ 20 counts s^{-1}, in the energy bands of 0.5–10 keV, 10–70 keV, and 70–400 keV, respectively. However, the true XIS 0 counts would be higher, if the data were free from telemetry overflows and event pile up (subsection 2.2).

2.2. XIS Data Selection

We retrieved XIS data that were prepared via version 1.2 processing. The XIS data were further screened based on the following standard criteria: the XIS GRADE should be 0, 2, 3, 4, or 6; the time interval after an exit from the South Atlantic

Anomaly should be longer than 500 s; and the object should be at least 5° and 20° above the dark and sunlit Earth rim, respectively.

In order to conduct spectral and timing studies, we utilize XIS events extracted from a region that is defined to fit in the "1/8 window". Since the Suzaku attitude is known to wobble on a time scale of several tens of minutes, the region needs to be a little smaller than the window size. Considering the magnitude of the wobbling, we defined the region as an intersection between a rectangle of 70×1024 pixels and a circle with a radius of $3{.}'3$ (200 pixels), both centered always on the image peak. For this purpose, we calculated the image center every 200 s and re-defined the event extraction region also every 200 s. Thus, the location of the region on the CCD chip is time dependent. Because the background was entirely negligible throughout the observation (less than 0.1% of the signal at 8 keV considering the Galactic ridge emission), it was not subtracted from the data.

Because Cyg X-1 was so bright, we needed to carefully remove the effects of telemetry saturation and photon pile up. When the number of detected events exceeded the telemetry allocation to the XIS, the excess events were discarded without being transferred to telemetry. This phenomenon is called telemetry saturation. Since the event buffer was cleared every 8 s, and the XIS exposure was 1 s in the present observation, we excluded the telemetry-saturated data in the following way. For each 8-s window, we calculated an average count rate over the first 4 s, which is usually free from the telemetry saturation. If a subsequent exposure in the same 8-s window showed a count rate lower than this average by more than 2 standard deviations, we judged that the telemetry was saturated, and discarded this and the subsequent exposures in the same window. This typically occurred in the last one or two exposures in the 8-s window. Because these telemetry-saturated time bins are regarded as dead times, the source count rate remains approximately intact, although the exposure is reduced.

After filtering out the telemetry-saturated data, we further removed the effects of photon pile up. Although the Suzaku X-ray telescopes have relatively wide point spread functions, photon pile up becomes noticeable at the image center when observing a point source brighter than ~ 100 counts per exposure. The average count rate of Cyg X-1 during the present observation was ~ 3 times higher than this limit. We therefore accumulated XIS events by excluding circular regions of various radii at the image center, and examined the obtained series of spectra for shape changes. As a result, we decided to exclude an image-center region with a radius of $1{.}'0$ (60 pixels). Although this means that the event extraction region has a complicated shape (intersection of an annulus and a rectangle), we use standard ancillary response files (`ae_xi0_xisnom4_20060615.arf`, etc.) defined for a circular region of $4{.}'0$ radius. This is because the point spread function of the telescope has little energy dependence, and hence the spectrum would not change, except in normalization. We confirmed this inference using the data of a moderately bright point source, SS Cyg observed on 2005 November 2, and found that the spectral normalization should be multiplied by a factor of ~ 0.092 compared with that of PIN, when excluding the central $1'$ of the image; this was taken into

account in the subsequent spectral analysis. We also used the standard response matrices (`ae_xi0_20060213.rmf`, etc.) for the XIS.

2.3.   HXD Data Selection and Background Subtraction

The HXD data utilized here were prepared via version 1.2 processing. We further screened the HXD events by imposing conditions that more than 500 s should be elapsed from an exit out of the South Atlantic Anomaly, that the target should be $> 5°$ above the Earth rim, and that the geomagnetic cutoff rigidity should be higher than 8 GV.

Since the HXD has neither imaging capability nor an offset counter to measure instantaneous non X-ray background (NXB), we need to estimate the NXB and to subtract it from the raw data. Accordingly, we employed the PIN background modeling by S. Watanabe et al. (2007),[1] known as "PINUDLC (bgd_a)" model,[2] which combined actual HXD-PIN data acquired while pointing to night Earth (Kokubun et al. 2007). Thus, we produced a large number (10.0 times as large as the actual) of fake non X-ray background events, which would just be detected during the present observation if we had an imaginary NXB monitor detector. By processing fake event files exactly in the same manner as the actual data, we can estimate NXB contributions in the PIN data, and subtract them from PIN light curves as well as from PIN spectra, with a typical accuracy of 5%, or better. The cosmic X-ray background entering through the PIN field of view was entirely negligible in the present study.

Subtraction of the HXD-GSO background employs a different method, developed by Y. Fukazawa et al. (2007)[3] and called "LCFIT (bgd_d)" model.[4] In this case, the whole GSO energy band is divided into 32 energy bins, and a light curve of each energy bin is produced over a long period. Because each light curve has characteristic repetition patterns with periods of one orbital revolution, one day (due to the relation with respect to the South Atlantic Anomaly), and 51 d (due to orbital precession), it can be expressed as a function of time using a relatively small number of adjustable parameters. The parameters can be determined by analyzing these light curves over a long period, typically one month. We can thus derive the expected NXB counts in individual energy bins at a given time during the present observation, and subtract them either from light curves or spectra. The GSO data are hence analyzed using the same energy binnings as used in the NXB modeling. When integrated over ~ 1 d, this method reproduces the GSO background within a systematic error of $\sim 2\%$ (H. Takahashi et al. 2007).[5] Since the PIN and GSO background models both utilize PIN upper-discriminator hit rates, their basic time resolution is typically 4 s or longer, depending on the telemetry rate.

1   Watanabe, S., Ushio, M., Tanaka, T., Kokubun, M., Fukazawa, Y., & the HXD team 2007, ⟨http://www.astro.isas.jaxa.jp/suzaku/doc/suzakumemo/suzakumemo-2007-01.pdf⟩.

2   ⟨http://www.astro.isas.jaxa.jp/suzaku/analysis/hxd/hxdnxb/⟩.

3   Fukazawa, Y., Watanabe, S., Kokubun, M., & the HXD team 2007, ⟨http://www.astro.isas.jaxa.jp/suzaku/doc/suzakumemo/suzakumemo-2007-02.pdf⟩.

4   ⟨http://www.astro.isas.jaxa.jp/suzaku/analysis/hxd/gsonxb/⟩.

5   Takahashi, H., et al. 2007, ⟨http://www.astro.isas.jaxa.jp/suzaku/doc/suzakumemo/suzakumemo-2006-43.pdf⟩.
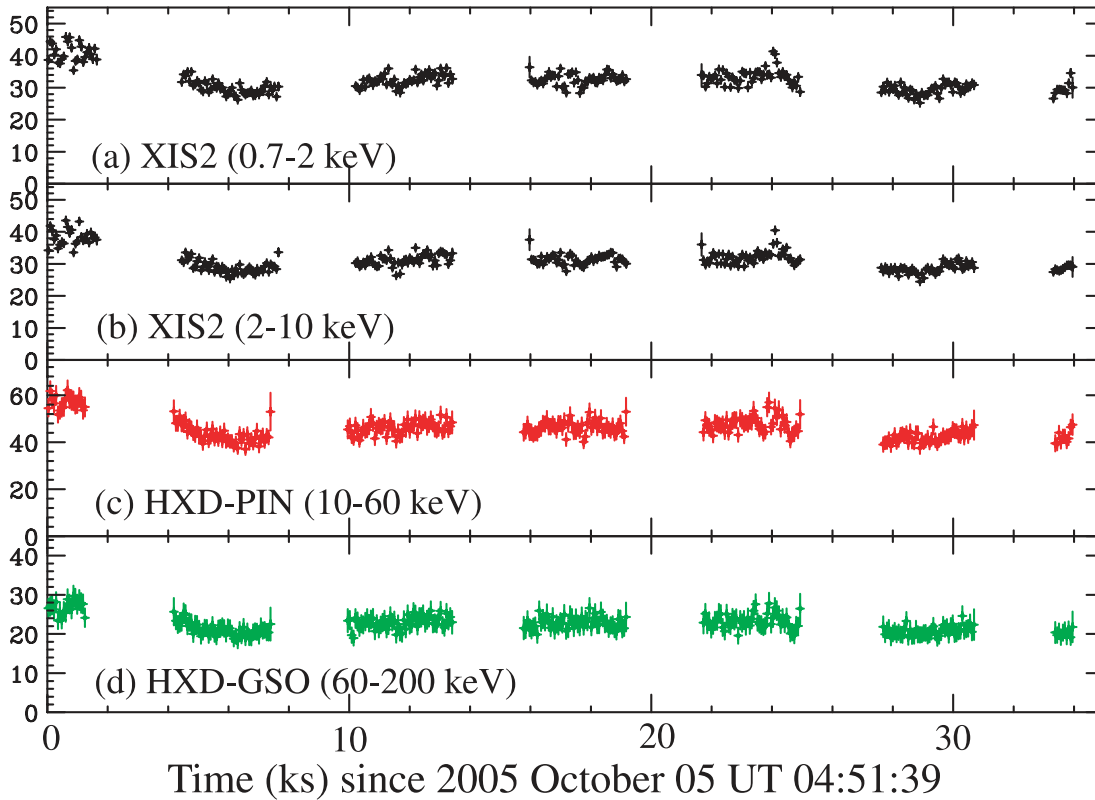
Fig. 1. Light curves of Cyg X-1 binned into 64 s, obtained in the present Suzaku observation performed in 2005 October. The ordinates are in units of counts s^{-1}. From top to bottom, the panels refer to those obtained with XIS 2 (0.7–2 keV), also with XIS 2 (2–10 keV), with HXD-PIN (10–60 keV), and with HXD-GSO (60–200 keV). The HXD backgrounds were subtracted. The periodic data gaps are due to spacecraft passages through the South Atlantic Anomaly and the Earth occultation.

2.4. Light Curves

Figure 1 shows XIS 2, HXD-PIN, and HXD-GSO light curves of Cyg X-1 from the present observation. The HXD backgrounds (PIN and GSO) were subtracted in the way described in subsection 2.3; the results were corrected for dead times. In contrast, the XIS background, which is completely negligible, is inclusive. The count rates indicated by these XIS light curves are by an order of magnitude lower than those actually observed, because of the image-center exclusion that was needed to avoid pile-up events (subsection 2.2). On time scales of a few minutes to a day, the source thus varied randomly, typically by $\sim \pm 10\%$.

2.5. Time-Averaged Spectra

We show in figure 2 the time-averaged Suzaku spectra of Cyg X-1. Like in subsection 2.4, we corrected the HXD spectra for the dead times, and subtracted the backgrounds using the method described in subsection 2.3. In contrast, the XIS 2 spectrum is here and hereafter not corrected for the normalization reduction (down to 0.092 of the original level), due to exclusion of the central 1′ of the images (subsection 2.2). For a comparison, we superpose the modeled background spectra of HXD-PIN and HXD-GSO.

As can be seen in figure 2, we significantly detected Cyg X-1 nearly across the full energy band of Suzaku. In particular, the source signals in HXD-PIN exceed the NXB by more than a factor of ~ 5, even at the highest energy of ~ 70 keV.
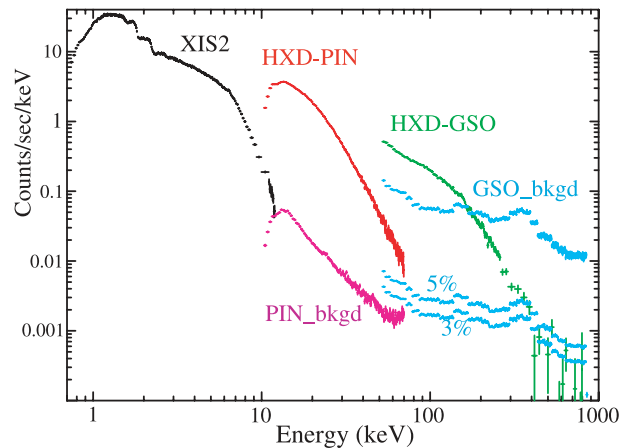

Fig. 2. Time-averaged XIS 2 (black), HXD-PIN (red), and HXD-GSO (green) spectra of Cyg X-1, shown after subtracting the background, but not removing the instrumental responses. The XIS 2 spectrum is accumulated after removing the telemetry overflow and cutting off the image center (see text). The modeled non X-ray background of HXD-PIN is indicated in magenta. That of HXD-GSO is shown in cyan, together with its 5% and 3% levels.

Therefore, the systematic background uncertainty of HXD-PIN is completely negligible compared to photon counting statistics. Even in the GSO range, the source signal is so strong that it can be detectable up to ~ 400 keV, above which the systematic background errors start to dominate.

3. Analysis of the Time Averaged Spectra

This section is devoted to a study of time-averaged Suzaku spectra of Cyg X-1. Because of the strong telemetry saturation (subsection 2.1), we do not use the data from XIS 1 (BI). Of the three FI CCD cameras comprising the XIS, only the data from XIS 2 are employed in our spectral analyses, while those from XIS 0 and XIS 3 are utilized in section 4 for a different purpose; even if we incorporated data from the other XIS sensors, systematic errors would dominate before data statistics are improved, because Cyg X-1 is so bright for the XIS.

3.1. Fitting with Conventional Models

In order to roughly characterize the time-averaged broadband spectra derived in subsection 2.5, we simultaneously fitted simple empirical models to the XIS 2, HXD-PIN, and HXD-GSO spectra, so that the results may be compared with other observations of Cyg X-1, as well as those of other similar objects. Here and hereafter, the overall model normalization is allowed to differ between the XIS and HXD (mainly to absorb uncertainties introduced by the removal of telemetry saturated data and the image-center exclusion), but constrained to be the same between HXD-PIN and HXD-GSO. As the detector responses, we use `ae_xi2_20060213.rmf` and `ae_xi2_xisnom4_20060615.arf` for the XIS 2, `ae_hxd_pinxinom_20060814.rsp` for the PIN, while `ae_hxd_gsoxinom_20060321.rsp` and `ae_hxd_gsoxinom_20070424.arf` for the GSO. The last GSO file is the correction factor described in Paper I, introduced so as to make the Crab Nebula spectrum described by a single PL model with $\Gamma = 2.1$.[6] We discard the XIS data in the 1.7–1.9 keV range so as to avoid the complexity of the Si-K edge modeling, and those in the > 8 keV band, which is possibly still affected by photon pile-up effects. The HXD-PIN data below 12 keV were also discarded in the fitting, to avoid response uncertainties there (Kokubun et al. 2007). We utilized the HXD-GSO data in the 70–400 keV energy band, because of the poor signal significance (figure 2) and relatively large response uncertainties, in > 400 keV and < 70 keV, respectively. We assigned a systematic error of 1% to all of the spectral bins, in order to absorb any uncertainties in the instrumental calibration, including in particular those associated with the detector responses and background estimation. The effect of contamination on the optical blocking filters of the XIS was modeled as additional absorption (Koyama et al. 2007). We also trimmed the energy offset by ~ 17 eV, while considering the current uncertainty with the XIS energy scale in the 2×2 mode.

As the simplest attempt, we first fitted an absorbed single PL model simultaneously to the three sets of spectra. The fit indicated $\Gamma \sim 1.77$ as the best estimate, and an absorbing hydrogen column density of $N_H = 3.5 \times 10^{21}$ cm^{-2}. However, the fit was far from acceptable, with $\chi^2/\nu = 14.3$ for $\nu = 360$ degrees of freedom. As can be seen in figure 3b, the fit leaves several noticeable discrepancies, including a prominent data deficit above ~ 100 keV, and a data excess in 0.9–1.5 keV. Obviously, the former is due to the high-energy cutoff, while the latter is due to the presence of soft excess, both of which have been established through previous observations.

To express the high-energy turnover, we next replaced the PL component with a cutoff power-law model (`cuoffpl`; a power-law times an exponential factor). To account for the soft excess, we also added a disk-blackbody component (`diskbb`: Mitsuda et al. 1984; Makishima et al. 1986) to our fitting model. The `diskbb` model is a simple non-relativisitic approximation to the X-ray spectrum integrated over a standard accretion disk, and is considered to provide an approximately (within ~ 10%: Watarai et al. 2000) correct innermost disk radius when an appropriate correction factor is incorporated (Kubota et al. 1998). Thus, the model is `wabs × (diskbb + cutoffpl)` in the xspec terminology; here, we utilized version 11 of the xspec spectral fitting package,[7] together with the photoelectric absorption model, `wabs`, by Morrison and McCammon (1983). Then, the fit was improved drastically to $\chi^2/\nu = 3.7$ for $\nu = 357$, though not yet acceptable. The exponential cutoff energy was obtained as $T_{cut} \sim 170$ keV, and the nominal PL photon index decreased to $\Gamma \sim 1.45$. The innermost disk temperature of the `diskbb` component was obtained as $T_{in} \sim 0.5$ keV, and its innermost radius as $r_{in} \sim 13$ km at a distance of 2.5 kpc (section 1), without any correction for the color hardening factor, or inner boundary condition, or inclination (see Makishima et al. 2000). We regard these `diskbb` parameters as still being unphysical.

In figure 3c, the data-to-model ratios from the `wabs × (diskbb + cutoffpl)` fit show a slight broad hump over 20–40 keV (though not very clear in this presentation), indicative of reflection from a cool thick material. In addition, there is clear evidence of an Fe-K line at about 6.4 keV. Accordingly, we added a reflection component (`pexrav`: Magdziarz & Zdziarski 1995) and a Gaussian to our model, thus constructing a model `wabs × (diskbb + cutoffpl + pexrav + gau)`, and repeated the fitting. In using `pexrav`, the reflector was assumed to have an inclination of $i = 45°$, and its incident photons to have the same spectral shape and normalization as those of the `cutoffpl` continuum (`rel_refl` < 0 technically). The Gaussian was allowed to have a free centroid and a free width. Then, the fit further improved to $\chi^2/\nu = 2.4$ for $\nu = 353$, implying that the reflection is significantly present as reported by many previous observations. The model gave the `cuoffpl` parameters as $\Gamma \sim 1.74$ and $T_{cut} > 1000$ keV, and the `diskbb` parameters as $T_{in} \sim 0.3$ keV and $r_{in} \sim 45$ km. The reflector was found to have a moderate solid angle as $\Omega/(2\pi) \sim 0.5$, and the Gaussian centroid and its width were obtained as 6.43 keV and $\sigma < 0.2$ keV respectively. In figure 3a, we show this fit where contributions of the individual model components are separately drawn. The data-to-model ratios are given in figure 3d. Thus, the reflection signal is inferred to carry ~ 30% of the continuum at 30 keV.

In this way, the empirical model fittings have roughly quantified the time-averaged Suzaku spectra of Cyg X-1, and extracted their basic features. The fit implies a 0.7–300 keV flux (after absorption by N_H) of 5.4×10^{-8} erg cm^{-2} s^{-1}. Assuming an isotropic emission, and employing a distance

---

[6] ⟨http://www.astro.isas.jaxa.jp/suzaku/analysis/hxd/gsoarf/⟩.

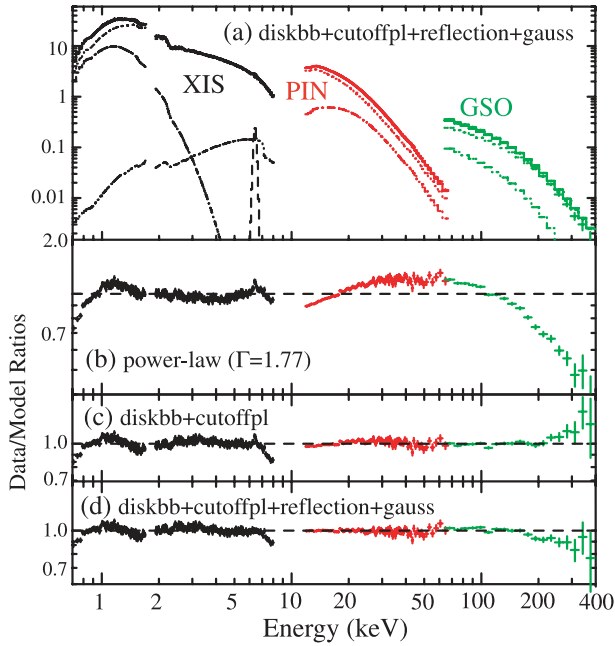[7] ⟨ttp://www.heasarc.gsfc.gov/docs/xanadu/⟩.

Fig. 3. Simultaneous fittings to the time-averaged XIS 2, HXD-PIN, and HXD-GSO spectra of Cyg X-1, using various combinations of conventional models. (a) Background-subtracted and response-inclusive spectra (the same as in figure 2), compared with the best-fit model consisting of a disk-blackbody, a cutoff power-law, a Gaussian, and a reflection component, i.e., wabs × (diskbb + cutoffpl + pexrav + gau). Individual model components are separately drawn. (b) Data-to-model ratios for an absorbed single-PL fit. (c) The same as panel b, but a disk-blackbody component is added, and the power-law is replaced by a cutoff power-law model. (d) The data-to-model ratios corresponding to the fit in panel a, namely, obtained by further adding to the model of panel c a Gaussian and a reflection component.

of 2.5 kpc (section 1), the absorption-removed 0.7–300 keV luminosity becomes 4.6×10^{37} erg s^{-1}, which is typical of this object. Although the fit still remains unacceptable, and hence errors associated with the model parameters cannot be evaluated, further improving the model would be of little meaning, because cutoffpl is a mere empirical approximation to the spectra expected from unsaturated Comptonization processes. Instead, we proceed to more physical modelings, using theoretical Comptonization codes.

3.2. Fitting with Comptonization Models

Among various Comptonization codes currently available, here we employ that of Poutanen and Svensson (1996), called compPS in xspec, because of the following three advantages: it correctly takes into account the relativistic effects in the Compton-scattering kinematics; it allows us to use a diskbb model as the seed photon source; and it has a built-in function to allow a part of the initial Compton-produced photons to get into a cold matter and reflected.

We thus fitted the XIS 2, HXD-PIN, and HXD-GSO spectra simultaneously by a wabs × (diskbb + compPS) model, in the same manner as before. At this stage, the reflection option in compPS was suppressed, and the Gaussian component was not included. Here and hereafter, we assume that the Compton cloud has a spherical geometry (parameter = 4) with an

electron temperature T_e and an optical depth τ, and that the seed photons to the compPS component are supplied by a cool standard disk having the same T_{in} (but a separate normalization) as the diskbb component. The implied picture is that some fraction of photons from a standard disk is fed to the Comptonizing corona, while the rest is directly visible as the spectral soft excess. This picture is supported by the presence of a tight correlation between the continuum slope and the reflection strength in BHBs (Zdziarski et al. 1999; Gilfanov et al. 1999; Revnivtsev et al. 2001) and in AGNs, which indicates that the optically thick disk, producing the reflection, is also causally related to the Comptonized emission.

As shown in figure 4b, this model gave a poor fit with $\chi^2/\nu = 3.9$ for $\nu = 357$. Since figure 4b reveals the reflection hump at ~ 30 keV, we activated the reflection option in compPS. This has nearly the same effect as the pexrav model, but with two additional free parameters: the ionization parameter ξ in units of erg cm s^{-1}, and the innermost reflector radius R_{in}^{ref}. The latter controls relativistic blurring of the spectral features, and is expressed in units of the gravitational radius, $R_g = GM_{BH}/c^2$, with M_{BH} the BH mass and G the gravitational constant. The outer radius was fixed at $10^6 R_g$ and the radial emissivity profile was assumed to depend on the radius r as r^{-3} (Fabian et al. 1989). The inclination angle, abundance, and temperature of the reflector were also fixed at 45°, 1 solar, and 10^6 K, respectively. We retained the Gaussian component, because the compPS reflection does not include any emission line. Then, as shown in figure 4c, the fit was much improved ($\chi^2/\nu = 2.6$ with $\nu = 351$); the reflection hump is significantly present with $\Omega/(2\pi) \sim 0.2$ and $\xi \sim 0$, although R_{in}^{ref} was not constrained in this and all subsequent fits. The fit goodness is comparable to that obtained with the wabs × (diskbb + cutoffpl + pexrav + gau) model (figure 3d). While the conventional model failed to constrain T_{cut}, the present model gave an electron temperature of $T_e = 115$ keV.

In figure 4c, the fit still leaves a prominent data deficit in the highest XIS range. In addition, the XIS vs. HXD normalization ratio was obtained at 0.108, which exceeds the nominal value of ~ 0.092 (subsection 2.2); this is too large, even considering uncertainties in the correction factors involved in the XIS and HXD data processing (section 2). We hence suspect that the actual source continuum is rising from ~ 10 keV toward lower energies, with a steeper slope than indicated by the model, so that the fitting algorithm tried to absorb this mismatch by artificially raising the model prediction to the XIS data. In other words, the broad-band continuum has a more concave shape over 2–20 keV (see figure 3b), than would be explained by the compPS component with reflection. This effect was previously noticed by Di Salvo et al. (2001) as a soft excess that cannot be accounted for by the cool disk emission. The same effect was noticed in the Suzaku data of GRO J1655−40 (Paper I), and led Takahashi et al. (2008) to incorporate another compPS component. Such a "double-Compton" modeling was previously applied successfully to the LHS of Cyg X-1 in several works; by Gierliński et al. (1997) and Ibragimov et al. (2005) using simultaneous Ginga, RXTE, and CGOR/OSSE data, and by Frontera et al. (2001a) to the BeppoSAX data.

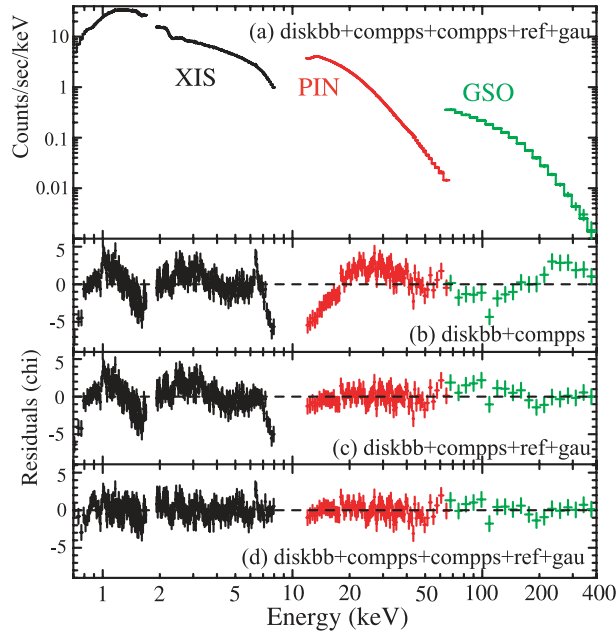We hence tried a model incorporating two Comptonized

Fig. 4. Simultaneous fittings to the time-averaged XIS 2, HXD-PIN, and HXD-GSO spectra of Cyg X-1, employing thermal Comptonization models. The derived best-fit parameters are given in table 1. (a) The same spectra as in figure 3a, compared with the best-fit `wabs` × (`diskbb` + `compPS` + `compPS` + `gau`) model. The two `compPS` components are constrained to have the same T_e, and a common set of reflection parameters. (b) Fit residuals from a model incorporating a single `compPS` continuum without reflection, together with a `diskbb`. (c) The same as panel b, but reflection is incorporated, and a Gaussian for the Fe-K line is added. (d) The residuals correspond to the fit shown in panel a. Compared to panel c, the second `compPS` component is added.

continua, which are constrained to have the same seed-photon temperature (which in turn is the same as that of `diskbb`), the same hot-electron temperature, and the same reflection parameters, but are allowed to differ in their normalization and optical depth. The model is hence `wabs` × (`diskbb` + `compPS` + `compPS` + `gau`). As shown in figure 4d, the fit was been improved drastically to $\chi^2/\nu = 1.13$ ($\nu = 349$); the XIS, PIN, and GSO spectra are reproduced with $\chi^2/\nu = 1.3$, 0.9, and 0.9, respectively. The model removed the data deficit in the highest XIS range, and reduced a residual structure near 2 keV, where the two `compPS` components now cross over. Furthermore, the XIS vs. HXD normalization became 0.088, which is close to the value of 0.092 calibrated using SS Cyg (subsection 2.2). We are therefore confident that the Suzaku data require two (or possibly more) Compton components. Although the fit is not yet formally acceptable, we regard it as being satisfactory, because the data vs. model discrepancy, typically within 4% over the entire 0.7–400 keV range, is comparable to those obtained when we fit the Suzaku spectra of bright objects, such as the Crab spectra, with simple models.

Our final model obtained in this way is shown in figure 4a in the convolved form, and in figure 5a in the incident $\nu F\nu$ form. Its model parameters are given in table 1. Hereafter, we call the `compPS` components with the larger and smaller y-parameters `compPSh` and `compPSs`, respectively, with the
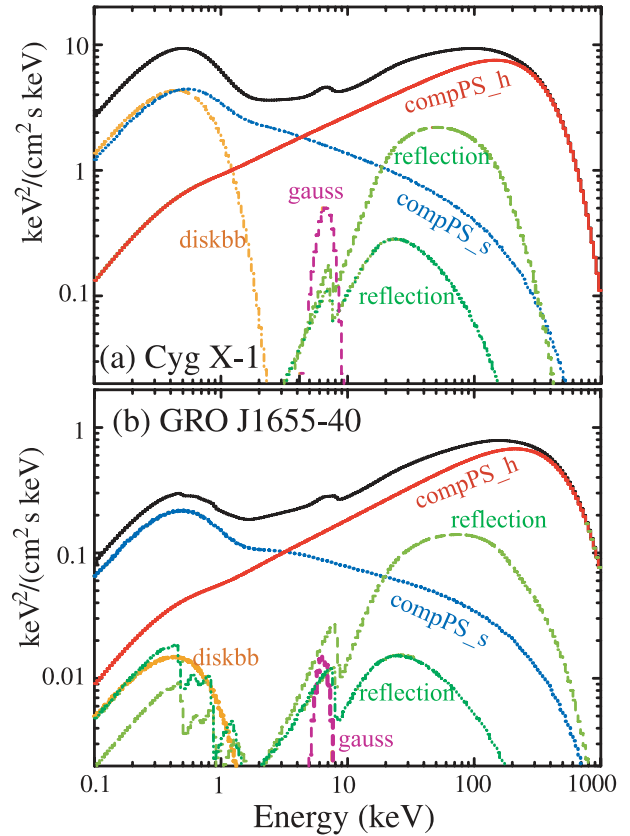

Fig. 5. (a) Inferred best-fit $\nu F\nu$ spectrum of Cyg X-1, shown with the absorption removed. It corresponds to panels a and d of figure 4, with the model parameters detailed in the column labeled "Average" of table 1. Red, blue, orange, green, and purple specify `compPSh`, `compPSs`, `diskbb`, reflection components, and a Gaussian for the Fe-K line, respectively. (b) The same as panel a, but for GRO J1655−40 observed with Suzaku on 2005 September 22 and 23. It is identical to figure 7 of Paper I, except for the removal of the absorption.

suffix "h" standing for "hard" and "s" for "soft". In figure 5, the `compPSs` component includes not only the scattered photons [$\propto 1 - \exp(-\tau)$], but also those seed photons that traversed the Compton cloud without being scattered [$\propto \exp(-\tau)$].

3.3. Examination of the Comptonization Model Results

Although the analysis conducted in the preceding subsection has provided a plausible representation of the time-averaged spectra, different spectral models could often degenerate. Therefore, let us briefly examine our final spectral model for its implications and physical consistency, leaving any detailed discussion to section 5.

The obtained absorption, $(6.6^{+0.8}_{-0.3}) \times 10^{21}$ cm^{-2}, is close to the value of $(5.3 \pm 0.2) \times 10^{21}$ cm^{-2}, derived by Dotani et al. (1997) with ASCA. The `compPSh` and `compPSs` components, crossing at ~ 4 keV, are characterized by photon indices of ~ 1.6 and ~ 2.4, respectively, with the former consistent with the approximate X-ray slope of Cyg X-1 measured in energies of a few to a few tens keV. The underlying parameters, $T_e \sim 100$ keV, τ of order unity, and $\Omega/(2\pi) \sim 0.4$, are consistent with a large number of past measurements (e.g., Gierliński et al. 1997; Di Salvo et al. 2001; Frontera et al.

Table 1. Simultaneous fits to the XIS 2, HXD-PIN, and HXD-GSO spectra of Cyg X-1 using two thermal Comptonization components.*

Component	Parameter	Average	High phase	Low phase	Difference	GRO J1655−40[†]
wabs	$N_{\rm H}$ (10^{21} cm^{-2})	$6.6^{+0.8}_{-0.3}$	(6.6 fix)	(6.6 fix)	(6.6 fix)	$7.4^{+0.3}_{-0.1}$
diskbb	$T_{\rm in}$ (keV)	$0.19^{+0.01}_{-0.02}$	0.19 ± 0.01	0.18 ± 0.01	(0.19 fix)	0.18 ± 0.01
	$R_{\rm in}$ (km) [‡]	250^{+210}_{-60}	250^{+30}_{-150}	270^{+50}_{-40}	< 110	< 73
	$L_{\rm raw}$ [§]	10^{+13}_{-3}	11^{+1}_{-9}	10 ± 1	< 2	< 1
compPSh	$T_{\rm e}$ (keV)	100 ± 5	95^{+15}_{-5}	105^{+10}_{-15}	60^{+10}_{-15}	140 ± 10
	optical depth	$1.49^{+0.07}_{-0.09}$	$1.5^{+0.2}_{-0.3}$	$1.4^{+0.4}_{-0.1}$	$2.0^{+0.5}_{-0.4}$	1.14 ± 0.08
	y-parameter	$1.15^{+0.05}_{-0.03}$	$1.12^{+0.03}_{-0.09}$	$1.17^{+0.11}_{-0.03}$	0.89 ± 0.3	$1.31^{+0.11}_{-0.08}$
	$R_{\rm in}^{\rm seed}$ (km)[‖]	75 ± 10	80^{+15}_{-10}	75^{+10}_{-15}	45 ± 5	26^{+5}_{-4}
compPSs[#]	optical depth	$0.38^{+0.04}_{-0.05}$	$0.38^{+0.07}_{-0.22}$	$0.32^{+0.21}_{-0.05}$	0.4 ± 0.2	$0.25^{+0.02}_{-0.03}$
	y-parameter	$0.29^{+0.04}_{-0.03}$	$0.28^{+0.03}_{-0.14}$	$0.27^{+0.11}_{-0.03}$	$0.16^{+0.09}_{-0.04}$	$0.28^{+0.07}_{-0.05}$
	$R_{\rm in}^{\rm seed}$ (km)[‖]	200^{+90}_{-30}	210^{+80}_{-10}	210^{+40}_{-20}	130^{+15}_{-30}	64^{+7}_{-10}
reflection**	$\Omega/(2\pi)$	$0.4^{+0.2}_{-0.3}$	(0.4 fix)	(0.4 fix)	(0.4 fix)	0.5 ± 0.1
	ξ (erg cm s^{-1})	< 30	(0 fix)	(0 fix)	(0 fix)	400 ± 100
	$R_{\rm in}^{\rm ref}$ ($R_{\rm g}$)	2500[††]	(2500 fix)	(2500 fix)	(2500 fix)	> 200
Gaussian	centroid (keV)	6.3 ± 0.1	$6.3^{+0.1}_{-0.2}$	$6.3^{+0.1}_{-0.2}$	(6.3 fix)	$6.3^{+0.1}_{-0.2}$
	eq. width (eV)	290 ± 90	290 ± 50	330^{+60}_{-50}	400 ± 200	100^{+10}_{-20}
	sigma (keV)	$1.0^{+0.1}_{-0.2}$	$0.9^{+0.2}_{-0.1}$	1.1 ± 0.2	(1.0 fix)	0.7 ± 0.1
fit goodness	χ^2_ν (ν)	1.13 (349)	1.08 (228)	1.17 (193)	1.01 (64)	1.03 (1484)
figure		figures 4a,d	figure 9a	figure 9b	figure 9c	Paper I

* Cyg X-1 and GRO J1655−40 are assumed to be at distances of 2.5 kpc and 3.2 kpc, respectively. The fitting model is wabs × (diskbb + compPS + compPS + gauss).

[†] The results on GRO J1655−40 refer to Paper I.

[‡] The innermost disk radius derived via equation (1), assuming $i = 45°$ for Cyg X-1 and $i = 70°$ for GRO J1655−40.

[§] Bolometric luminosity in 10^{36} erg s^{-1}, obtained as $L_{\rm raw} = 4\pi R_{\rm in}^2 \sigma_0 T_{\rm in}^4$ with σ_0 the Stefan–Boltzmann constant.

[‖] Square root of the compPS normalization, converted to the inner radius of the seed photon disk via equation (2). Note this is not divided by the $\sqrt{\cos i}$ factor.

[#] Assumed to have the same $T_{\rm e}$ as compPSh.

** The parameters are assumed to be common to the two compPS components. The reflector inclination is assumed in the same way as in [‡].

[††] Not constrained in the fitting.

2001a; Zdziarski & Gierliński 2004; Ibragimov et al. 2005).

The diskbb component has a raw innermost radius as of $r_{\rm in} = 180^{+150}_{-50}$ km, which yields the best-estimate actual inner radius of $R_{\rm in} = 250^{+210}_{-60}$ km; this is obtained by applying the nominal correction factors in Makishima et al. (2000) (including a color hardening factor of 1.7; Shimura & Takahara 1995) to $r_{\rm in}$, and correcting for the inclination assuming $i = 45°$, as

$$R_{\rm in} = 1.18 r_{\rm in} / \sqrt{\cos i} . \qquad (1)$$

This $R_{\rm in}$ is larger than the value of $R_{\rm in} \sim 100$ km measured in the high/soft state with ASCA (Dotani et al. 1997; Makishima et al. 2000), suggesting a disk truncation at a larger radius than in the high/soft state (see also subsection 5.4). The innermost disk temperature, 0.19 keV, is a factor 2.3 lower than that measured in the high/soft state (Dotani et al. 1997), consistent with a reduced accretion rate and possibly a larger innermost disk radius. These consistencies support (though not necessarily prove) our basic assumption that the seed photons for Comptonization are provided by the optically-thick disk, as proposed previously (Zdziarski et al. 1999; Gilfanov et al. 1999; Revnivtsev et al. 2001). Although the bolometric luminosity of the directly-visible disk emission is 19^{+24}_{-6}% of the overall 0.7–300 keV luminosity, the energy generation in the cool disk is approximately twice higher, when the seed photon luminosity is added. Then, the energy generation in the cool disk becomes comparable to that in the hot corona.

While the compPSh component carries the dominant hard continuum, compPSs successfully explains the continuum steepening in energies below a few keV, or equivalently the soft excess that is too hot to be explained by the cool disk emission (Di Salvo et al. 2001). These two Compton continua are inferred to have optical depths that differ by a factor of 3.9 ± 0.5. Their normalizations, originally expressed as the disk area A supplying the seed photons, have been converted in table 1 to the innermost radius $R_{\rm in}^{\rm seed}$ as

$$R_{\rm in}^{\rm seed} = 1.18 \sqrt{A} . \qquad (2)$$

Though similar to $R_{\rm in}$ of equation (1), $R_{\rm in}^{\rm seed}$ is *not* corrected for the inclination, since we presume the Comptonized emission to be approximately isotropic. As can be seen in table 1, the value of $R_{\rm in}^{\rm seed}$ associated with compPSs is comparable to $R_{\rm in}$, while that of compPSh is considerably smaller. We hence obtain an implication that ~ 7 times more seed photons are fed to compPSs than to compPSh; a further discussion continues in subsection 5.4.

Although the final model is generally successful, the obtained XIS vs. HXD normalization, 0.088, is $\sim 5\%$ too small. When this ratio is fixed to the calibration value of 0.092, the PIN data exhibit some positive and negative residuals at $\sim 15\,\text{keV}$ and $\sim 40\,\text{keV}$, respectively. These can be eliminated by allowing `compPSs` and `compPSh` to have a larger (~ 1.0) and a slightly smaller (~ 0.3) value of $\Omega/(2\pi)$, respectively, with the raw chi-square reducing by 13 (for $\nu = 349$). This is because the reflection associated with `compPSs` appears at lower energies than those with `compPSh` (figure 5a). There is thus some indication that the softer Compton signals are more strongly reflected by cold materials than the harder one.

When the two `compPS` components are allowed to take different values of T_e, the tolerances of the model parameters increase, but the fit goodness remains the same. This is because the high-energy roll over of `compPSs` is masked by `compPSh`. Therefore, we do not adopt this modeling, although the data do not necessarily exclude the presence of multiple electron temperatures.

4. Analysis of Spectral Changes Associated with the Random Variation

4.1. Methods

Now that the time-averaged spectra have been quantified in section 3, we proceed to the latter half of our data analysis, namely attempts to understand how the spectrum changes as the source varies randomly; a similar attempt was carried out previously by Takahashi, Inoue, and Dotani (2001). For this purpose, it is essential to sort the broad-band spectra, particularly those of the HXD, into two subsets, according to whether the instantaneous source count rate is higher or lower than a certain mean value. However, the HXD has a relatively small effective area ($\sim 230\,\text{cm}^2$ at $100\,\text{keV}$: Takahashi et al. 2007), so the average count rates of Cyg X-1 are $\sim 47\,\text{counts s}^{-1}$ and $\sim 20\,\text{counts s}^{-1}$ in the 10–70 keV (with PIN) and 70–400 keV (with GSO) bands, respectively (subsection 2.1; figures 1c, 1d). Then, even in the PIN range where the NXB is relatively minor, Poisson fluctuations of signal counts with 1 s integration would become comparable to the intrinsic variations of Cyg X-1 ($\sim \pm 20\%$ in root-mean-square amplitude). Making the integration time longer would not help, because Cyg X-1 varies with an approximately "white" power spectrum on time scales longer than a few seconds (e.g., Belloni & Hasinger 1990), and hence the amplitudes of the intrinsic and Poisson variations will scale in a similar manner when the integration time is increased.

Fortunately, we can utilize the XIS for our purpose, because one XIS sensor received $\sim 60\,\text{counts s}^{-1}$ even after the image center has been removed to avoid photon pile up (subsection 2.2; figures 1a, 1b), and the variation of Cyg X-1 is known to be crudely synchronized across the soft X-ray to hard X-ray energies (Negoro et al. 1994). Since the present XIS data have a 1 s time resolution (subsection 2.1), we can judge every second, by referring to the XIS data, whether the source is brighter or fainter than a mean, and sort the XIS and HXD data into the required two subsets. In practice, we have constructed the following procedure to do this:

1. In the same way as in subsection 2.4, a 0.3–10 keV XIS 0 + XIS 3 light curve $\{C_i\}$ (with i the bin number) is produced throughout the observation, with a bin width of $t_b \geq 1\,\text{s}$.
2. The calculation of $\{C_i\}$ excludes those 1-s time bins in which either XIS 0 or XIS 3 (or both) suffered telemetry saturation.
3. Every $T\,\text{s}$ ($T \gg t_b$), the mean XIS 0 + XIS 3 count rate, $\bar{C}$, is calculated from $\{C_i\}$.
4. Two sets of good time intervals (GTIs), called "high-phase" (HP) and "low-phase" (LP), are defined by judging every $t_b\,\text{s}$ whether C_i is higher than $\bar{C} + n\sigma$, or lower than $\bar{C} - n\sigma$, respectively. Here, σ is the 1-sigma Poisson error and $n \geq 0$ is the discriminator level.
5. Using the same two GTIs, the XIS 2 data are accumulated into two spectra, called HP (high phase) and LP (low phase) spectra. The data are discarded if $\bar{C} - n\sigma < C_i < \bar{C} + n\sigma$.
6. Employing the same two GTIs, the HXD-PIN data are sorted into HP and LP spectra; so are the HXD-GSO data.
7. Using the two sets of GTIs, two background data sets are accumulated for HP and LP, and are subtracted from the corresponding on-source HXD spectra.

Thus, the procedure involves three adjustable parameters (t_b, T, and n). Among them, T should be long enough to suppress Poisson errors, but short enough to compensate for background changes. The threshold n should also be optimized, because a larger n leads to a decrease of the live time, while a smaller n means that the data sorting is diluted by the Poisson fluctuation in $\{C_i\}$, which is not related to the intrinsic source variation. Here, for simplicity we have chosen $t_b = 1\,\text{s}$ (the highest time resolution of the XIS), $T = 200\,\text{s}$, and $n = 0$ as our baseline conditions. This is because a larger value of n, such as $n = 1$, was found to enhance the HP vs. LP ratio, but also to degrade the data statistics, thus hampering us to more accurately separate the HP and LP model parameters. Since we have chosen to use the XIS 0 + XIS 3 data for the intensity judgement, we derive the intensity-sorted XIS spectra only from the other FI sensor, namely XIS 2. This division of task is needed because the intensity-sorted spectra from XIS 0 and XIS 3 would include those time bins when their summed counts are higher (or lower) due simply to statistical fluctuations, which amount to $\sim 8\%$ (1 sigma) at the 1-s integration. The intensity-sorted spectra from XIS 0 and XIS 3, if they are to be utilized in the spectral fitting, would need to be corrected for this effect. The XIS 2 data, in contrast, are free from this problem, because Poisson errors from different detectors are independent.

4.2. Auto-Correlation and Cross-Correlation Functions

Before actually conducting the analysis described in subsection 4.1, we briefly perform auto-correlation function (ACF) and cross-correlation function (CCF) analyses, in order to examine whether the GTIs sorted in reference to the energy band below 10 keV are really applicable to the extraction of varying spectral components in harder energies. We utilize raw light curves with neither background subtraction nor dead-time correction.
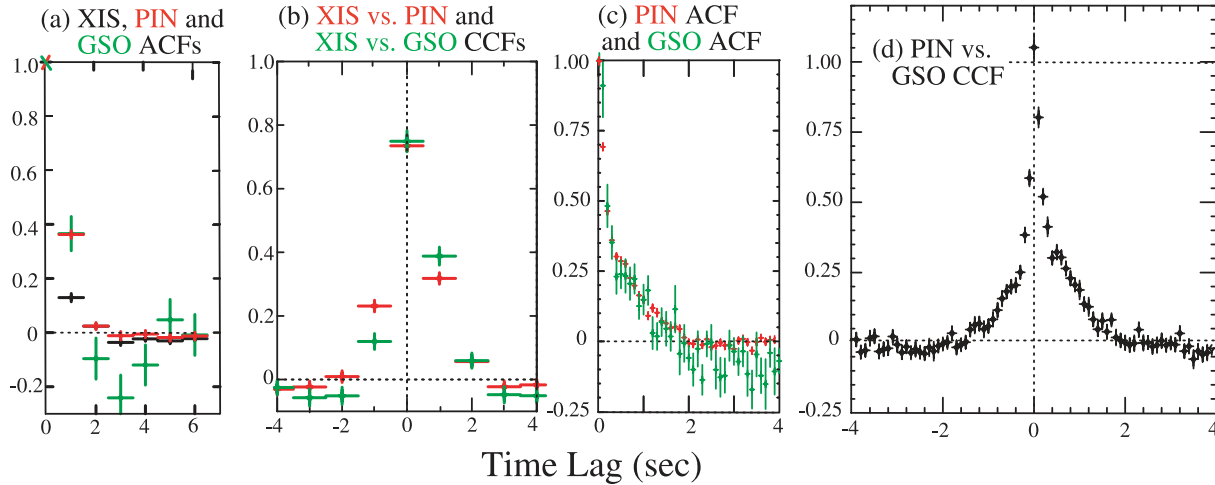
Fig. 6. Auto-correlation functions (ACFs) and cross-correlation functions (CCFs) of the present Suzaku data. The effects of Poisson errors were removed, and the CCFs were normalized so that the value at zero lag directly represent the correlation coefficient. Positive time differences in CCFs mean that softer signals lead the harder ones. (a) ACFs from the XIS 2 (0.7–10 keV; black), HXD-PIN (10–60 keV; red), and HXD-GSO (60–200 keV; green) data, calculated using 1-s binned light curves. (b) CCFs of the PIN (red) and GSO (green) data, calculated against the 0.7–10 keV XIS 2 light curve in the same way as panel a. (c) ACFs calculated using 0.1-s binned PIN (10–60 keV; red) and GSO (60–200 keV; green) light curves. (d) CCFs of the GSO light curve against that of PIN, calculated in the same way as panel c.

Panels (a) and (b) of figure 6 show ACFs and CCFs from the present Suzaku data, respectively, calculated employing a bin width of 1 s. They were calculated using data intervals each 256 s long, and then averaged over the ensemble. The XIS telemetry saturation was treated in the same way as item 2 of the previous subsection (using $t_b = 1$ s). Thus, the XIS vs. PIN and XIS vs. GSO CCFs both exhibit clear peaks at zero time lag, with correlation coefficients of ~ 0.75. This ensures that the intrinsic variation on a time scale of 1 s is well correlated over the entire energy range in which we are conducting our analysis, and validate our method described in the previous subsection.

Although the XIS data do not have time resolution higher than 1 s, the HXD data afford it down to 61 μs (Takahashi et al. 2007; Terada et al. 2008). We calculated ACFs and CCFs from the PIN (10–60 keV) and GSO (60–200 keV) light curves accordingly, with 0.1 s resolution and 409.6 s data intervals. The results, shown in panels (c) and (d) of figure 6, reveal that the variations are detected on shorter time scales, where the PIN vs. GSO correlation is still peaked at zero-lag. The variations in the two energy bands are again well synchronized, with the correlation coefficient of ~ 1.

In addition to the basic properties described above, these ACFs and CCFs reveal one interesting property: namely, the left-to-right asymmetry in the CCFs, seen on both time scales, in such a way that the correlation is stronger toward hard-lag sense. This reconfirms the previous report of the same phenomenon in early days by Nolan et al. (1981), then using Ginga by Miyamoto et al. (1992), and further with RXTE (e.g., Nowak et al. 1999b; Maccarone et al. 2000). On the other hand, the present results do not clearly reconform another property, reported previously (e.g., Negoro et al. 1994; Feng et al. 1999; Maccarone et al. 2000), that ACFs in softer energies have wider correlation peaks, and hence longer correlation lengths. We leave this issue to future Suzaku

observations using higher XIS time resolution (employing so-called PSUM mode); then, we will also be able to study how the spectrum differs between the rising and falling phases of "shots", as suggested previously (Negoro et al. 1994).

4.3. Intensity-Sorted Spectra

Now that the examination of CCFs have validated the method presented in subsection 4.1, we applied it to the present Suzaku data. Figure 7 gives an example of 1-s bin light curves of Cyg X-1, sorted according to the above method using the following baseline condition: $t_b = 1$ s, $T = 200$ s, and $n = 0$ (subsection 4.1). In this particular example, the average XIS count rate used as the HP vs. LP threshold is 140 and 148 counts s^{-1} in the former and latter 200 s, respectively. These are $\sim 15\%$ higher than the XIS 2 counting rate indicated by figure 1 (panels a, b), because the XIS 2 optical axis is more offset from the 1/8-window centroid than those of XIS 0 and XIS 3, causing a larger photon loss. The XIS light curve reveals the well-known flickering behavior of Cyg X-1, while those of the HXD suffer larger Poisson errors so that the intensity sorting on a time scale of 1 s is impossible without the XIS data.

Figure 8 shows the HP and LP spectra derived in this way. There, we subtracted the corresponding backgrounds accumulated using the respective GTIs (item 7 in subsection 4.1); the utilized two background sets agree within their statistical errors. While the spectra are presented without any dead-time correction, we corrected the model nomalizations (in table 1 and elsewhere in text) for a time-averaged dead time of 7%. Although the HP and LP spectra should have different dead times, the difference was calculated to be within $\sim 2\%$, because the dead time is mainly caused by background counts. This difference is expected to reduce the HP spectral normalization by at most 2%, while keeping the spectral shape intact.

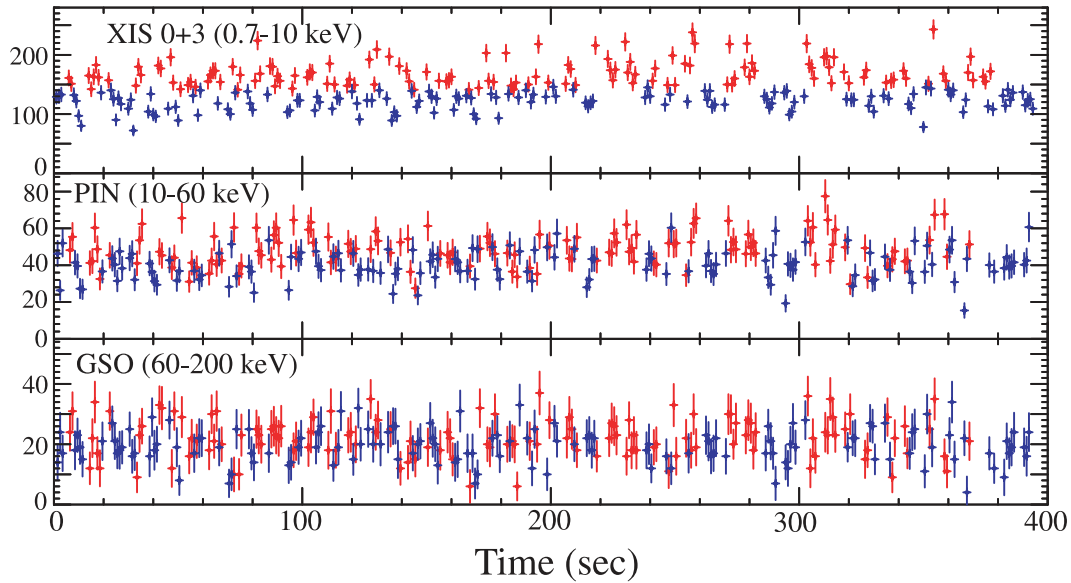Figure 8b gives the ratios between the HP and LP spectra,

Fig. 7. Background-inclusive XIS (top, 0.7–10 keV), HXD-PIN (middle, 10–60 keV), and HXD-GSO (bottom, 60–200 keV) light curves of Cyg X-1 with 1-s binning, sorted according to the instantaneous XIS 0 + XIS 3 counts. Red and blue data bins represent those when the XIS 0 + XIS 3 counts, C_i, are higher and lower than the local 200 s average, $\bar{C}$, respectively. No correction is made for the instrumental dead times.
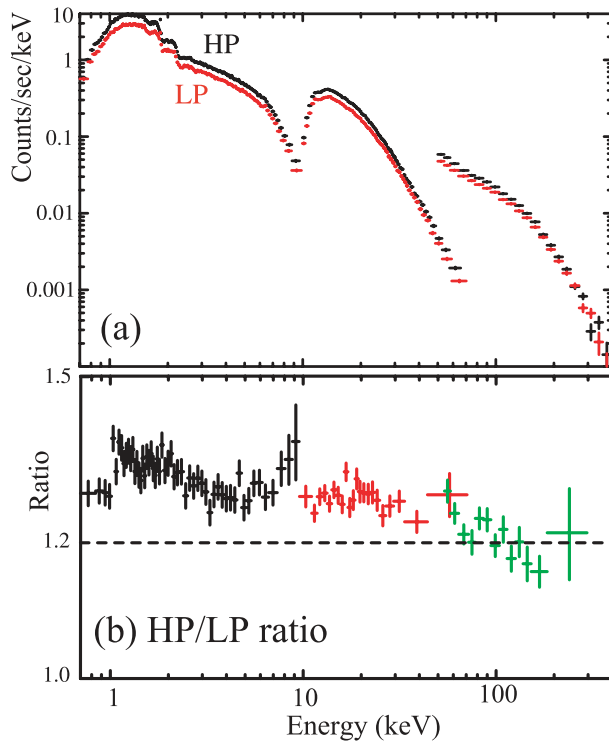

Fig. 8. (a) HP (high phase; black) and LP (low phase; red) spectra of Cyg X-1 recorded by XIS 2, HXD-PIN, and HXD-GSO, while XIS 0 + XIS 3 data are used in the intensity judgement. The corresponding HXD backgrounds have been subtracted. (b) Ratios between the HP and LP spectra.

effects in the XIS when the source gets brighter, and should be ignored. Third, the spectrum becomes slightly softer when the source brightens up, as evidenced by a gradual decrease of the HP/LP ratio toward higher energies; this qualitatively agrees with previous results from, e.g., Ginga (Negoro et al. 1994). Finally, the HP/LP ratio exhibits a rather abrupt decrease at ~ 1 keV toward lower energies.

In order to see the effects of changing the selection condition, we repeated the intensity sorting using $t_b = 3$ s and 8 s. The results obtained with $t_b = 3$ s were essentially the same as those with the baseline case ($t_b = 1$ s). When employing $t_b = 8$ s, the HP/LP ratio was reduced to ~ 1.2 on average, although its energy dependence was very similar to the baseline case. From these, we retained $t_b = 1$ s. We also examined different Poisson thresholds, n. When $n = 0$ (the baselline case), 1, and 2 were used, the HP GTIs yielded an overall exposure of 7.3, 5.2, and 3.3 ks, respectively (with LP GTI being comparable), while the energy-averaged HP/LP ratio turned out to be ~ 1.3, ~ 1.4, and ~ 1.5, respectively. We hence retained $n = 0$, since it maximizes the signal-to-noise ratio of the HP minus LP difference spectra.

Returning to the HP and LP spectra obtained with the baseline condition, we tried grossly quantifying them using the conventional model employed in subsection 3.1. To avoid the complexity in softer energies that arisses from the iron line, the soft excess, and the softer Compnotization continuum, we fitted only the HXD (PIN and GSO) spectra, using the `cutoffpl + pexrav` model. The model successfully reproduced the HP and LP spectra both with $\chi/\nu \sim 1$, and yielded a consistent reflection strength: $\Omega/(2\pi) = 0.16^{+0.05}_{-0.06}$ in HP and 0.16 ± 0.06 in LP. (These are smaller than the value of ~ 0.4 obtained with the time-averaged spectra using the Compnonization models, because a cutoff power-law model is more convex than an unsaturated Compton continuum.)

To highlight the difference between the two spectra, we next

with several important implications. First, the average ratio becomes ~ 1.3, in agreement with the typical variation amplitude of Cyg X-1. Second, the ratio increases at the highest XIS energies band, but this is due to still remaining photon pile-up

Table 2. Cutoff power-law fits to the HXD (PIN and GSO) spectra in HP and LP.*

Component	Parameter	Free	Common Γ	Common E_{cut}
cutoff PL	Γ (HP)	1.51 ± 0.02	1.51 ± 0.01	1.52 ± 0.01
	Γ (LP)	1.50 ± 0.02	—†	1.49 ± 0.01
	E_{cut} (HP)	212 ± 12	208^{+5}_{-8}	220 ± 10
	E_{cut} (LP)	234 ± 16	240 ± 12	—†
	Norm. ratio‡	1.31	1.27	1.39
fit goodness	χ_ν (ν)	0.93 (168)	0.93 (169)	0.94 (169)

* The HP and LP spectra were fitted simultaneously with the `cutoffpl+pexrav` model. The reflection strength was fixed at $\Omega/(2\pi) = 0.16$.
† Constrained to be the same between the HP and LP spectra.
‡ The ratio of `cutoffpl` normalization (at 1 keV) between HP and LP.

fitted them jointly, with $\Omega/(2\pi)$ fixed at 0.16. As show in table 2 (column under an entry "Free"), we were unable to find statistically significant differences either in Γ or E_{cut}. Therefore, we further constrained the HP and LP spectra to have either the same Γ or the same E_{cut}. Then, as shown in the last two columns of table 2, the joint fit remained acceptable without any preference between the two cases, and the unconstrained parameter showed a statistically significant difference between the two spectra. We therefore concluded that the HP and LP spectra have different shapes, as suggested by their ratio (figure 8b), and that either E_{cut} or Γ (or both) is changing, although we cannot determine which is more variable.

4.4. Changes of the Compton Parameters

Following an approximate quantification of the intensity-sorted HXD spectra (subsection 4.3), we fitted the full (XIS 2, PIN, and GSO) HP and LP spectra with the `wabs ×` `(diskbb + compPS + compPS + gau)` model, which has been found to be the best representation of the time-averaged spectrum (subsection 3.2). In the fitting, we fixed $N_H = 6.6 \times 10^{21}$ cm^{-2}, as obtained with the average spectra. In reference to the preliminary fittings conducted in the previous subsection, we also fixed all of the reflection parameters to the values obtained with the average spectra. Then, as presented in figure 9, the model has successfully reproduced both spectra. The derived parameters are listed in table 1, compared with those from the averaged spectrum. Thus, the LP and HP values of each free parameter (except a few rather unconstrained ones) are found to generally bracket that from the average spectrum. The inferred best-fit models, in the $\nu F\nu$ form, are given in figure 10.

Table 1 and figure 10 allow us to derive several important inferences. First, let us consider the observed spectral softening from LP to HP (figure 8b). Although this effect might suggest an increased relative contribution of `compPSs` in HP, this is not the case. In fact, as the source varies, the seed-disk radius of `compPSs` is kept at 3 ± 1 times that of `compPSh` (table 1), and their cross-over energy stays at ~ 4 keV (figure 10). In search for an alternative explanation, figure 11 compares the `compPSh` parameters between HP and LP on the plane of T_e against the optical depth, τ_h. Thus, the HP and LP spectra become distinct on this plane, with an implication similar to what was derived in subsection 4.3: the two phases cannot be represented by a common set of T_e and τ_h.
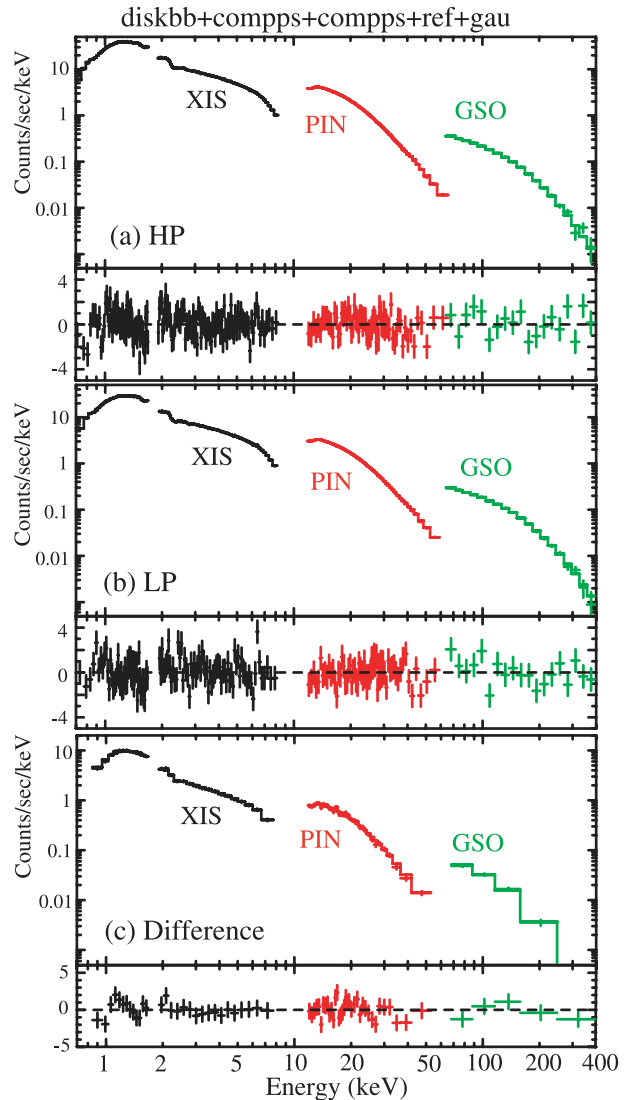

Fig. 9. Background-subtracted and dead-time uncorrected HP (panel a) and LP (panel b) spectra of Cyg X-1, fitted with the `wabs × (diskbb+compPS+compPS+gau)` model in the same way as in figure 4. Panel c is for the difference spectra between HP and LP.
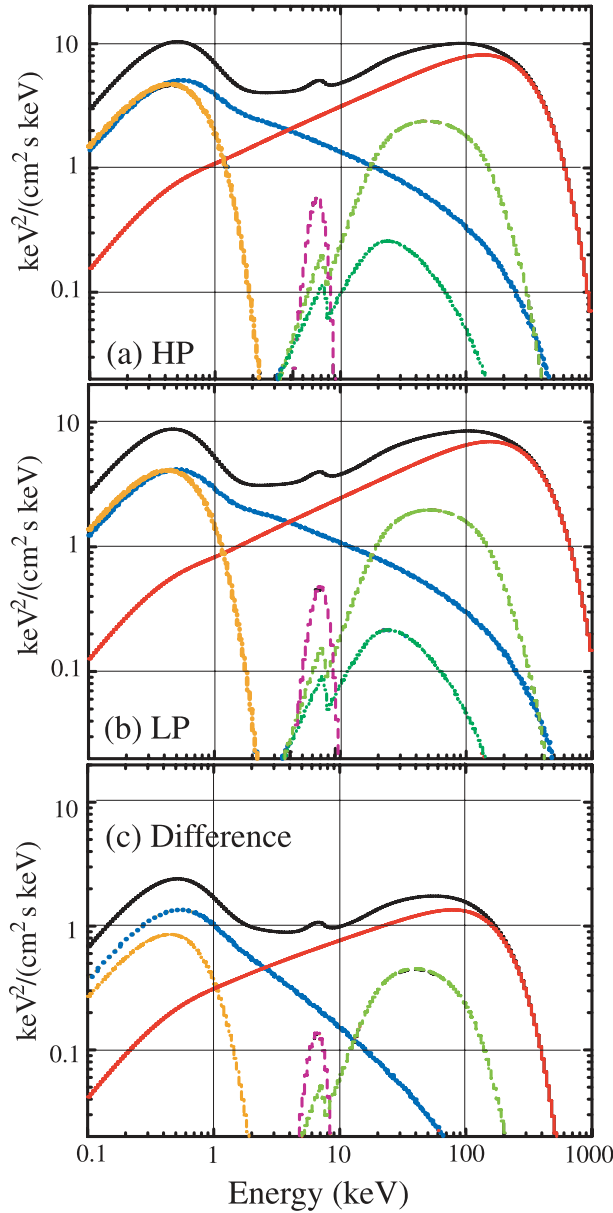
Fig. 10. Same as figure 5a, but obtained from the HP (panel a) and LP (panel b) spectra. Panel c is the fit to the HP minus LP difference spectra.
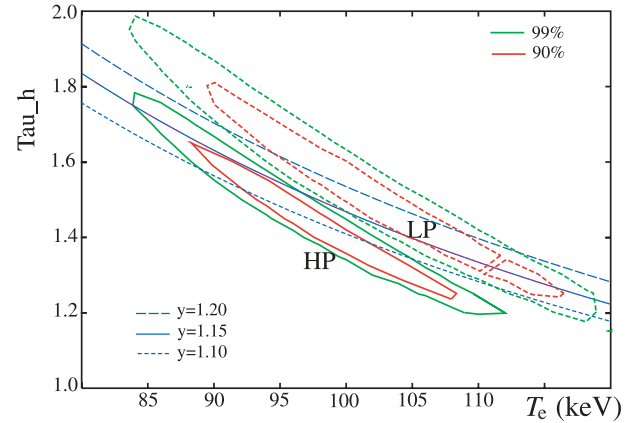

Fig. 11. Confidence contours of the `compPSh` paramters in HP (solid lines) and LP (dashed ones), shown on the plane of T_e versus the optical depth, τ_h. The red and green contours represent the 90% and 99% confidence levels, respectively. The blue lines indicate constant values of y.

the seed photon sources for the two `compPS` components. Therefore, it is determined mainly by local shapes of the spectral soft excess (figure 10). However, the broad-band capability is again very important, because it allows us to accurately fix the Compton continua and the reflection hump, and hence to unambiguously model the soft excess.

As a third result from this analysis, we can attribute the LP to HP intensity increase to an increase in the spherically-averaged seed-photon luminosity, which is given as

$$L_{\text{seed}} = 4\pi\sigma_0 T_{\text{in}}^4 \left(R_{\text{in-h}}^{\text{seed}2} + R_{\text{in-s}}^{\text{seed}2} \right) ; \qquad (3)$$

here, σ_0 is the Stefan-Boltzmann constant, while $R_{\text{in-h}}^{\text{seed}}$ and $R_{\text{in-s}}^{\text{seed}}$ respectively represent the seed-disk radius of `compPSh` and `compPSs`, as defined by equation (2). When L_{seed} is estimated in table 1 via equation (3), its nominal error ranges overlap between HP and LP, due to large errors in $R_{\text{in}}^{\text{seed}}$. However, in reality, $R_{\text{in}}^{\text{seed}}$ is tightly anti-correlated with T_{in} so as to preserve the seed-photon flux (for `compPS` in particular). Therefore, the combined error range of L_{seed} becomes much smaller. A detailed confidence-range examination yields $L_{\text{seed}} = (8.8^{+6.1}_{-0.8}) \times 10^{36}$ erg s^{-1} in HP, and $(6.9^{+0.7}_{-1.8}) \times 10^{36}$ erg s^{-1} in LP.

Finally, the bolometric luminosity of the directly-visible `diskbb` component, calculated after equation (3) as

$$L_{\text{raw}} = 4\pi\sigma_0 T_{\text{in}}^4 R_{\text{in}}^2 \qquad (4)$$

and presented in table 1, is consistent with being the same between LP and HP, within rather large errors that arise mainly via a strong coupling between `diskbb` and `compPSs`. These error ranges associated with L_{raw}, which also take into account the temperature vs. radius anti correlation, are such that a significant decrease (by as much as a factor of ~ 5) in L_{raw} from LP to HP is allowed, while its increase should not exceed $\sim 20\%$. We therefore infer, as our 4th result, that the directly visible disk luminosity is likely to be less variable than the hard X-ray flux, and there remains a possibility that it even anti-correlates with the hard X-ray flux.

If, e.g., T_e is the same, then τ_h must be lower in HP than in LP; if instead τ_h is assumed to be the same, T_e must be higher in LP. The two phases are more clearly (though not completely) separated in y, because it can be accurately specified by the observed spectral slopes. We may, for simplicity, express that the hard continuum is "less strongly Comptonized" in HP than in LP. This is an important result enabled by the broad-band capability of Suzaku. As for `compPSs`, we cannot find any significant differences between LP and HP beyond their relatively large errors.

Next, the source variation has been found to approximately conserve the innermost disk temperature at $T_{\text{in}} = 0.19$ keV (table 1). In the present modeling, this quantity is assumed to be common to the directly visible `diskbb` component, and

4.5. Difference Spectra

To reconfirm and reinforce the results obtained in the preceding subsection, we directly subtracted the raw (i.e., background-inclusive and dead-time uncorrected) LP spectra from those in HP. Since the source resides in either phase for a typical duration of several seconds, which is much shorter than the time scale of the NXB variation, we expect the NXB to accurately cancel out by this subtraction, making "difference spectra" free from the NXB modeling errors. In fact, over the highest energy of 530–600 keV where the signal is considered to be negligible ($< 1\%$ of the NXB), the HP minus LP count rate of HXD-GSO has been found to be $(-0.6 \pm 1.0)\%$ of the time-averaged mean rate. This also confirms that the potentially higher (by at most 2%; subsection 4.3) dead time in HP than in LP can be neglected. The derived difference spectra are presented in figure 9c. As expected, they have several times smaller normalizations than the HP and LP spectra, and are generally softer.

As before, we fitted the difference spectra using progressively complex Comptonization models, but fixing $N_{\rm H} = 6.6 \times 10^{22}\,{\rm cm}^{-2}$, $T_{\rm in} = 0.19\,{\rm keV}$, $\Omega/(2\pi) = 0.4$, $\xi = 0$, and $R_{\rm in}^{\rm ref} = 2500\,R_{\rm g}$. The systematic errors were not incorporated due to lower statistics. Then, a single `compPS` continuum, together with reflection and the `diskbb` component, gave a poor fit with $\chi^2/\nu = 3.36$ for $\nu = 67$. The fit goodness was improved to $\chi^2/\nu = 3.18$ ($\nu = 66$) by activating the Gaussian component, of which the center energy and the width are fixed at 6.3 keV and $\sigma = 1.0$ keV, respectively. Finally, by incorporating the second `compPS` component, the fit became fully acceptable ($\chi^2/\nu = 1.05$ for $\nu = 64$), yielding the parameters given in table 1 (column before the last). Thus, the model has again the same construction as those for the time-averaged, HP, and LP spectra. The best-fit model is presented in figure 9c in the convolved form, and in figure 10c in the incident $\nu F \nu$ form. Below, we examine the fit results.

In the difference spectra, the `compPSs` component has been found to again have an ~ 3-times larger seed-disk radius than `compPSh`. Since this ratio is close to those found in the average, HP, and LP spectra, we reconfirm that the soft-photon inputs to the two Compton clouds are varying roughly in proportion to each other. In contrast, the value of $T_{\rm e} \sim 60$ keV is considerably lower than was found before. One possible scenario from these results is that the Compton-cloud temperature in fact has a distribution, which becomes more weighted toward lower values as the source flares up, so that the difference can be approximated by a single lower temperature.

In subsection 4.3, we confirmed (though using the conventional model) that the HP and LP spectra have roughly the same $\Omega/(2\pi)$. This is reinforced by results obtained subsequently, namely the successful double-Compton modelings of the HP, LP, and the difference spectra, all with $\Omega/(2\pi)$ fixed at 0.4. Therefore, the reflection component is thought to be fully catching up with the continuum variations on the 1-s time scale. Also, the iron-line photon flux is clearly varying on this time scale; its variation is consistent with being directly proportional to the continuum flux, because all four spectra of Cyg X-1 presented in table 1 have, within errors, the same Fe-K line equivalent width of ~ 300 eV. These results are consistent

with Revnivtsev et al. (1999), who reported that the reflection features (Fe-K line and smeared edge) start failing to follow continuum variations above several Hz in frequency.

Although the fit to the difference spectrum incorporates the `diskbb` component, the final model given in table 1 does not necessarily require it; only an upper limit can be imposed on $R_{\rm in}$, because the softest end of the difference XIS spectrum can be accounted for by `compPSs` as well. We in fact confirmed that a negative normalization of `diskbb` (i.e., a decrease of this component from LP to HP) is allowed up to $\sim 40\%$ (in absolute value) of those in LP. This is consistent with the results obtained in the previous subsection.

4.6. Summary of Spectral Changes

Through the analyses presented in the preceding three subsections, the spectra changes associated with fast (1 to 200 s) intensity variations have been quantified in the following manner:

1. The intensity increase from LP to HP is explained by an increase in the seed-photon luminosity, $L_{\rm seed}$.
2. The spectral softening from LP to HP can be attributed to a weakening in the Comptonization of `compPSh` (either small τ, or lower $T_{\rm e}$, or both).
3. Unlike $L_{\rm seed}$, the directly visible disk luminosity, $L_{\rm raw}$, does not increase significantly in HP, and could even decrease.
4. As the source varies, the innermost temperature of the cool disk is kept approximately constant at $T_{\rm in} = 0.19$ keV.
5. On these time scales, the Fe-K line and the reflection hump follow the continuum variations, because $\Omega/(2\pi)$ and the Fe-K line equivalent width are both consistent with being constant.

5. Discussion

5.1. Summary of the Data Analysis

The Suzaku observation of Cyg X-1, conducted for an exposure of 17 ks at a 0.7–300 keV luminosity of $4.6 \times 10^{37}\,{\rm erg\,s}^{-1}$, has provided one of the highest-quality LHS spectra of this prototypical BHB. The XIS, HXD-PIN, and HXD-GSO spectra, altogether covering an extremely broad energy band of 0.7–400 keV, have been explained simultaneously and consistently, by invoking two basic constituents of the X-ray emission. One is the hot Comptonizing corona with $T_{\rm e} \sim 100$ keV, which manifests itself in the high-energy spectral roll over detected with a high significance by HXD-GSO. The other is the optically thick cool disk with $T_{\rm in} \sim 0.2$ keV, which produces the soft excess and the Fe-K line in the XIS band, as well as the reflection hump in the HXD-PIN band with $\Omega/(2\pi) \sim 0.4$.

The data are fully consistent with the cool disk supplying seed photons to the Compton cloud, although other possibilities may not be necessarily excluded. In the present modeling, the soft photons from the cool disk are considered to reach us either directly as soft excess (the `diskbb` component), or through weaker Comptonization with $y \sim 0.3$ (`compPSs`), or after experiencing stronger Comptonization with $y \sim 1.15$ (`compPSh`).

Assembling together the two Compton components (`compPSh, compPSs`) and the three cool-disk related ones (`diskbb`, reflection, and Gaussian), we have successfully reproduced the overall continuum shape, including the complicated Fe-K line and soft-excess regions. The Fe-K line is inferred to be broadened only weakly to $\sim 1\,$keV (in Gaussian σ), without any evidence for relativistically broadened wings of which the detection is claimed from some BHBs (Miller 2006). As can be seen in figure 5, the inferred incident spectrum shows too complicated a shape, all over the energy range, to be approximated by a single power-law.

Analyzing in section 4 the characteristic flare-up behavior of Cyg X-1 on a time scale of $\sim 1\,$s, we found that the `wabs × (diskbb + compPS + compPS + gau)` modeling also applies to the HP, LP, and the difference spectra. The flare-up behavior can be understood primarily as an increase in the seed-photon supply, accompanied by a decreased Comptonization. While the seed-disk luminosity thus increases in HP, the luminosity of the directly visible `diskbb` does not increase significantly. As the source varies, $T_{\rm in}$ of the cool disk is kept approximately constant.

5.2. Comparison with the BeppoSAX Results

Applying the double-`compPS` modeling to the BeppoSAX data of Cyg X-1 in the LHS covering up to $\sim 200\,$keV (whereas Suzaku reached $400\,$keV), Frontera et al. (2001a) derived $T_{\rm e} = 59 \pm 5\,$keV, $y = 0.89 \pm 0.01$, and $\Omega/(2\pi) = 0.25 \pm 0.04$ for `compPSh` (their Compton component 1), and $T_{\rm e} = 42 \pm 19\,$keV and $y = 0.15 \pm 0.01$ for `compPSs` (their `compPS` component 2). Except for some differences in the model parameters, the Suzaku and BeppoSAX results are hence consistent in that the broad-band spectra can be reproduced by a pair of Comptonized components. The two results grossly agree on the soft-excess parameters as well, although Frontera et al. (2001a) used a blackbody to model the soft excess and the seed-photon source.

The BeppoSAX observation was conducted at a 0.5–$200\,$keV unabsorbed flux of $4.2 \times 10^{-8}\,$erg cm^{-2} s^{-1}, or a luminosity of $3.1 \times 10^{37}\,$erg s^{-1} (in the same band at a distance of 2.5 kpc). The corresponding values from the present Suzaku observation are higher, $5.9 \times 10^{-8}\,$erg cm^{-2} s^{-1} ($4.4 \times 10^{37}\,$erg s^{-1}). Then, we would expect Suzaku to observe a lower $T_{\rm e}$, based on the general understanding that $T_{\rm e}$ decreases toward higher luminosities due to enhanced Compton cooling (e.g., Esin et al. 1998; Yamaoka et al. 2005; Zdziarski & Gierliński 2004). Nevertheless, we in fact measured a 1.6 times *higher* $T_{\rm e}$ than BeppoSAX. One possible explanation for this behavior is that Cyg X-1 may not have fully returned to the LHS at the time of the BeppoSAX observation, which was conducted soon after the source transition from the high/soft state.

Prior to the present work, the double-Compton model was successfully applied to wide-band LHS spectra of Cyg X-1 (Gierliński et al. 1997; Frontera et al. 2001a; Ibragimov et al. 2005; though some explicitly invoking multiple values of $T_{\rm e}$) and GRO J1655−40 (Paper I, subsection 5.3). Therefore, we regard this model as being a promising description of the LHS spectra of BHBs. As discussed in Paper I, the mixture of two Compton optical depths (plus the direct `diskbb` component) allows either a "spatial" or a "time-domain" interpretation. In

the former case, some fraction of the cool disk is considered to be directly visible, while the remaining part is covered by a hot electron cloud that has thinner and thicker portions. The latter (time domain) alternative assumes that the Compton cloud is rapidly varying among three typical conditions, represented by $\tau = 0$, $\tau \sim 0.4$, and $\tau \sim 1.5$. The actual condition may be a combination of these two simplified cases. Of course, as pointed out previously (e.g., Paper I), the double-Compton modeling may be an approximation to more complex conditions involving more than two Compton optical depths, or even a continuous distribution in τ, as suggested by some models (e.g., Liu et al. 2002). With the present data, it is virtually impossible to distnguish, which is more likely, a continuous distribution occurs in τ, or just two optical depths.

5.3. Comparison with GRO J1655−40

A comparison between Cyg X-1 (with $i \sim 45°$) and GRO J1655−40 (with $i \sim 70°$) would help to elucidate the source geometry (section 1). After a brief attempt made in Paper I using the BeppoSAX results on Cyg X-1 (Frontera et al. 2001a), here we perform a more accurate comparison between the two objects using the Suzaku data on both. For this purpose, figure 5b reproduces the best-fit `wabs × (diskbb + compPS + compPS + gau)` model for GRO J1655−40, deduced in Paper I using the Suzaku data. On that occasion (2005 September 22 and 23), GRO J1655−40 was in the LHS with a 0.7–$300\,$keV luminosity of $4.9 \times 10^{36}\,$erg s^{-1} (Paper I), which is an order of magnutude lower than that of Cyg X-1 in the present observation (both assuming isotropic emission). However, the difference becomes a factor of 3–5 when the luminosity is normalized to the Eddington value, because the BH in Cyg X-1 has a mass of 12–$20\,M_\odot$, while that in GRO J1655−40 has $\sim 6.5\,M_\odot$ (Paper I).

Although the two models in figure 5 generally look alike, they differ in details. To grasp such differences in a model-independent manner, we divided the XIS 2, HXD-PIN, and HXD-GSO spectra of GRO J1655−40 by the corresponding spectra of Cyg X-1, and obtained the results shown in figure 12. Below, we attempt to identify the basic features in this spectral ratio, and to interpret them in terms of the spectral decomposition in figure 5 and table 1. Like in figure 8b, the behavior of the ratio at the highest XIS energy range should be ignored, where the GRO J1655−40 data may suffer from photon pile-up effects (Paper I).

The spectral ratio in figure 12 is roughly constant over ~ 3 to $\sim 30\,$keV, but decreases significantly below $\sim 2\,$keV. This effect is too large to be explained by their difference in absorption, $N_{\rm H} = 6.6 \times 10^{21}\,$cm^{-2} in Cyg X-1 and $7.4 \times 10^{21}\,$cm^{-2} in GRO J1655−40. Instead, it can be attributed to the stronger soft excess of Cyg X-1 (figure 5), since the `diskbb` component of Cyg X-1 is an order of magnitude more prominent than that of GRO J1655−40 when normalized to the overall continuum (while $T_{\rm in}$ is nearly the same). This in turn may be ascribed primarily to their difference in the $\cos i$ factor, $\cos(45°)/\cos(70°) = 2.1$, because we expect the direct disk emission to scale as $\propto \cos i$, while the Comptonized emission to be approximately isotropic. Strictly speaking, this estimate needs some caution. In subsection 4.4, we introduced two quantities, $L_{\rm raw}$ and $L_{\rm seed}$. Because $R_{\rm in}$ used to calculate $L_{\rm raw}$
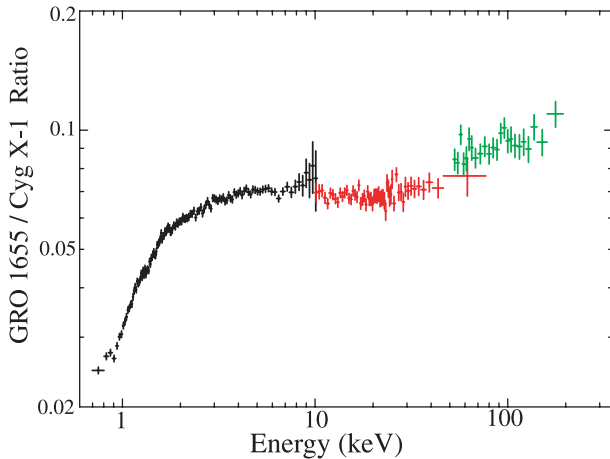
Fig. 12. Background-subtracted XIS (black), HXD-PIN (red), and HXD-GSO (green) spectra of GRO J1655−40 (Paper I), divided by those of Cyg X-1 obtained in the present study.

has already been corrected for the $\cos i$ factor, while R_{in}^{seed} has not (subsection 3.2, table 1), we expect the ratio L_{raw}/L_{seed} to be approximately inclination independent. Nevertheless, the ratio was measured to be ~ 0.44 in Cyg X-1, while < 0.19 in GRO J1655−40 (table 1). That is, the soft excess in GRO J1655−40 is even weaker than would be predicted by the assumed $i = 70°$. This is discussed later in subsection 5.5.

In figure 12, we observe a small dip at ~ 6.5 keV. Evidently, this feature arises because the Cyg X-1 spectrum exhibits a stronger Fe-K line (with an equivalent width of ~ 300 eV) than that of GRO J1655−40 (~ 80 eV). This property is again ascribed, at least qualitatively, to the inclination effects: the cool flat disk will intercept a fraction of the Comptonized photons, and produce fluorescent Fe-K photons, of which the visibility must be proportional to $\cos i$. Quantitatively, however, the difference in the equivalent width between the two sources amounts to a factor of ~ 4, which exceeds the factor of ~ 2 difference expected from $i = 70°$. This is also discussed in subsection 5.5.

Over the 30–200 keV range, the ratio in figure 12 increases with the energy E roughly as $\propto E^{0.3}$: GRO J1655−40 has a harder continuum. This is consistent with the PL approximation to their hard X-ray spectra, which gave $\Gamma = 1.75$ for Cyg X-1 (subsection 3.1) and $\Gamma = 1.39$ for GRO J1655−40 (Paper I). In terms of the Comptonization scenario, this slope difference can be attributed to the higher y-parameter of `compPSh` in GRO J1655−40 ($1.31^{+0.11}_{-0.08}$) than in Cyg X-1 ($1.15^{+0.05}_{-0.03}$). This in turn can be explained rather securely by the higher T_e of GRO J1655−40, unlike the case of the HP vs. LP comparison of Cyg X-1, in which the origin of the change in y remained ambiguous. As discussed in Paper I and subsection 5.2, the higher T_e of GRO J1655−40 may be due to its lower luminosity.

In the PIN energy range, the ratio of figure 12 exhibits a slightly concave curvature. Because the continua themselves in this energy range should be simple power-laws dominated by `compPSh`, this effect must be caused by differences in the reflection features. In fact, figure 5 reveals two

effects. One is that the reflection hump of Cyg X-1, relative to the Compton continuum, is inferred to be stronger than that in GRO J1655−40. This is again considered to be an inclination effect, because the reflected component is expected to be proportional to $\cos i$, while the primary continuum is thought to be rather isotropic. Actually, the values of $\Omega/(2\pi)$ in table 1, which were calculated *after correcting* for $\cos i$, become comparable between the two objects. The other effect is that the reflection hump in Cyg X-1, modeled with $i = 45°$, emerges at 30–50 keV, whereas that of GRO J1655−40, modeled with $i = 70°$, is peaked at higher energies. This is because a larger i makes the reflection more forward directed, and hence the reflected photons suffer less Compton degradation (Magdziarz & Zdziarski 1995). These two effects in combination are considered to produce a slightly concave-shaped spectral ratio in the PIN band. Incidentally, the comparable values of $\Omega/(2\pi)$ between the two objects disfavor the idea that the hot Comptonizing corona may have a semi-relativistic outflow velocity away from the disk plane (Malzac et al. 2001), because in that case we would observe a smaller value of $\Omega/(2\pi)$ from Cyg X-1 due to the enhanced continuum.

To summarize, the spectra of Cyg X-1 and GRO J1655−40 are both dominated by the Comptonized continua, but Cyg X-1 exhibits more prominently the flat-disk-related spectral features, presumably due to its lower inclination. Another inclination effect manifests itself in the subtle differences in the 10–70 keV continuum shape, presumably due to inclination-dependent changes in the strength and peak energy of the reflection hump. These results are consistent with the view that the Comptonizing hot cloud is geometrically thick, and hence its emission depends much less on the inclination than the flat-disk related components.

Analyzing broad-band BeppoSAX spectra of XTE J1118+480, Frontera et al. (2001b) discovered that this transient BHB has a very weak soft excess and a weak reflection hump. Like the present discussion on GRO J1655−40, these properties of XTE J1118+480 may also be ascribed to inclination effects, since this object is also reported to have a rather high inclination as $i = (68 \pm 2)°$ (Gelino et al. 2006).

5.4. The Disk Parameters in the Low/Hard State

In the high/soft state of Cyg X-1, a `diskbb` fit to the ASCA data showed the optically-thick disk to have $r_{in} = 71$ km (Dotani et al. 1997), which translates via equation (1) to $R_{in} = 90$ km for $i = 30°$ (Makishima et al. 2000) or $R_{in} = 100$ km for $i = 45°$. The disk is securely considered to reach the last stable orbit (Dotani et al. 1997; Makishima et al. 2000). In the LHS, a similar cool disk is considered to be present as well, but its conditions become significantly more difficult to estimate, because its emission is overwhelmed and strongly modified by the Compton process. As a result, there is considerable controversy over the innermost disk radius in the LHS.

Theoretically, the Advection Dominated Accretion Flows (ADAF: Narayan & Yi 1995) and other related hot flow models, meant to explain the LHS, all assume that the cool disk is truncated at some radius larger than the last stable orbit. (One important difference is that the original ADAF model assumes synchrotron photons as the soft seed photons to be Compton up-scatterd into hard X-rays, whereas the present

scenario assumes the cool disk to supply the seed soft photons.) A gradual inward shift in this truncation radius will give rise to the correlated spectral softening, increased reflection, and increased variation power frequencies, as observed (e.g., Gilfanov et al. 1999; Zdziarski et al. 1999, 2004; Zdziarski & Gierliński 2004; Done et al. 2007). When the disk reaches the last stable orbit, a transition to the high/soft state will take place. However, this view has been challenged by some LHS observations, which suggest that the disk extends down to the last stable orbit (Miller et al. 2006a, b; Rykoff et al. 2007). Here, we use the broad-band Suzaku data to infer the disk parameters in the LHS.

In subsection 3.1, the conventional `diskbb + cutoffpl` fit to the present LHS data tentatively gave $r_{in} \sim 13$ km, and hence $R_{in} = 18$ km for $i = 45°$. This apparently implies that the cool disk extends down to a much smaller radius than in the high/soft state. However, as pointed out before (Ebisawa et al. 1996; Di Salvo et al. 2001; Ibragimov et al. 2005), and revealed by the present data (figure 5), the LHS spectra of Cyg X-1 and other BHBs are significantly more complex than described by a single power-law. In fact, our final solution invoking double `compPS` has given an order-of-magnitude larger value, $R_{in} = 250$ km (table 1), which is consistent with the disk inner radius receding by a factor 2.5, compared to the high/soft state. The large difference in R_{in} between the two modelings for the same data can be explained in the following manner. In our final model, the flux in the 1–2 keV range is mostly explained by `compPSs` (figure 5a), with `diskbb` carrying softer residuals. If, instead, a single straight continuum is employed, the `diskbb` component becomes unusually hot because it tries to explain the 1–2 keV excess (Di Salvo et al. 2001; Ibragimov et al. 2005), and hence the inner disk radius becomes apparently too small. This gives a lesson that disentangling the disk parameters, where the disk is not the dominant component in the spectrum, is subject to large uncertainties in the underlying continuum shape. Evidently, the case of GRO J1655−40 is subject to larger difficulties because of the weaker soft excess.

The Comptonization scenario involves another important effect, which artificially reduces the disk radius: the disk photons are "lost" from the `diskbb` component into the dominant Comptonized continua. In estimating the true disk radius, to be denoted R_{in}^{tot}, we must take this effect into account, knowing that Comptonization conserves the photon number (Kubota et al. 2001; Kubota & Makishima 2004; Kubota & Done 2004). Practically, R_{in}^{tot} can be derived by quadratically summing R_{in} of `diskbb`, R_{in}^{seed} of `compPSh`, and R_{in}^{seed} of `compPSs` as

$$\left(R_{in}^{tot}\right)^2 = R_{in}^2 + \left(R_{in-h}^{seed}\right)^2 + \left(R_{in-s}^{seed}\right)^2 . \quad (5)$$

Then, equations (3), (4), and (5) readily yield the total luminosity, L_{disk}, of the cool disk as

$$L_{disk} = L_{raw} + L_{seed} = 4\pi \left(R_{in}^{tot}\right)^2 \sigma_0 T_{in}^4 . \quad (6)$$

From the values in table 1 for the time-averaged spectrum, we obtain $R_{in}^{tot} \sim 330$ km, which is equivalent to $\sim 15 R_g$ for $M_{BH} = 15 M_\odot$. The implications are that roughly half the disk area is directly visible, and the disk inner radius is factor 3 larger than in the high/soft state.

Although the estimated value of R_{in}^{tot} may still be relatively small compared with the original idea of disk truncation, it can be subject to yet additional uncertainties, which take part in when transforming the raw `diskbb` normalization into a physical radius. The stress-free inner boundary condition is probably appropriate for a thin disk extending down to the last stable orbit. In contrast, a truncated disk may have continuously rising stress to its inner radius. Similarly, the environment of the disk is different between the two states: in the LHS, the disk is likely to be more strongly heated by irradiation and conduction from the hot cloud. Therefore, the color hardening factor in the LHS may well be significantly larger than the value of 1.7 employed in equation (1); then, the true effective temperature would be lower, and hence R_{in} would become still larger.

Three independent pieces of evidence further argue against the small disk radius in the LHS. One is the relatively small values of reflection, $\Omega/(2\pi) \sim 0.4$, which requires the cool seed disk not to intrude too deeply into the hot corona. To reconcile the small values of $\Omega/(2\pi)$ with a configuration wherein the seed disk is nearly completely surrounded by the corona, we would have to invoke, e.g., mild relativistic coronal outflows (e.g., Malzac et al. 2001), but we already argued against it (subsection 5.3). Second, the intrinsic width of the Fe-K line, when interpreted as relativistic broadening in the disk near the BH, can constrain the innermost locations of the cool disk. For this purpose, we re-fitted the average spectra with the final model, but with the Gaussian replaced by so-called `diskline` model (Fabian et al. 1989). When fixing the inclination at 45°, and assuming the line emissivity to scale as r^{-3}, the fit constrained the rest-frame line center energy as $6.3^{+0.2}_{-0.1}$ keV, and the innermost disk radius for the Fe-K line production as $13^{+6}_{-7} R_g$ which is fully consistent with the value of $R_{in}^{tot} \sim 15 R_g$ derived above. Finally, as quoted in subsection 4.5, Revnivtsev et al. (1999) studied fast variations of Cyg X-1 in the Fe-K line energy region, and argued the cool reprocessor to be located farther than $\sim 100 R_g$ for $M_{BH} = 15 M_\odot$. Although the implied radius is much larger than considered here, this should be taken as another evidence supporting disk truncation. (Incidentally, the present results concerning the fast variability in the Fe-K lines and the Compton humps constrain their production sites to be closer than $1.3 \times 10^4 R_g$.)

Based on these examinations, we estimate that the cool-disk radius of Cyg X-1 during the present LHS observation is $R_{in}^{tot} \sim 15 R_g \sim 330$ km nominally, but is subject to rather large uncertainties, and is likely to be considerably larger than this.

All of the considerations presented here will also apply to previous LHS studies, where the small inner disk radius derived from simple continuum fits was used to challenge the truncated disk model (Miller et al. 2006a, b; Rykoff et al. 2007). In short, the small disk radii claimed for some BHBs in the LHS would need a careful revision.

5.5. A Possible Interpretation of the Fast X-Ray Variation

The remaining issue is how to interpret our results on the time variation, summarized in subsection 4.6 and subsection 5.1. In a standard accretion disk which we believe is approximately correct in the present case, the disk parameters are mutually related as $T_{in} \propto \left(R_{in}^{tot}\right)^{-3/4} \dot{M}^{1/4}$ (e.g., Makishima

et al. 2000), where $\dot{M}$ is the mass-accretion rate. Since T_{in} has been confirmed to change little as Cyg X-1 varies, the variation must also keep $R_{\text{in}}^{\text{tot}}$ and $\dot{M}$ approximately constant. (An alternative case, namely, positively correlated changes in $R_{\text{in}}^{\text{tot}}$ and $\dot{M}$, would be unlikely, because an increase in $\dot{M}$ would enhance radiative cooling, and hence *reduce* $R_{\text{in}}^{\text{tot}}$; Zdziarski et al. 1999; Zdziarski & Gierliński 2004; Done et al. 2007.) As a result, the total disk luminosity L_{disk}, defined by equation (6), should also be kept rather constant. However, L_{seed} has been found to increase from LP to HP (subsection 4.4). Therefore, L_{raw} must decrease in HP by 20–30%. As confirmed in subsections 4.4 and 4.5, the data permit (though do not require) such a decrease in L_{raw} from LP to HP.

Based on the above arguments, we presume that Cyg X-1 gets brighter as a larger fraction of the disk photons are intercepted by the Comptonizing corona, while the underlying cool disk itself is kept essentially unchanged. This will cause an increase in L_{seed}, and an associated decrease in L_{raw}. Although this inference does not necessarily specify how the corona is actually changing, we may consider one possible scenario below.

Let us, for example, assume that the Compton cloud has a rather spherical shape, or a thick torus geometry, with its outer radius located at $R_{\text{cc}} \sim 100\ R_{\text{g}} \sim 2 \times 10^3$ km, where the free-fall time is ~ 0.1 s. (The actual in-fall time scale of the corona may well be longer, depending on the viscosity.) Based on our discussion made in subsection 5.4, the cool disk is considered to partially protrude into the corona, but truncated at, say, $R_{\text{in}}^{\text{tot}} \sim 50\ R_{\text{g}}$. Comptonization will then take place both in the overlapping region (between $R_{\text{in}}^{\text{tot}}$ and R_{cc}), and inside $R_{\text{in}}^{\text{tot}}$, of the corona. The corona is assumed to be rather turbulent with strong density inhomogeneities, so that we need two optical depths, $\tau_{\text{s}} \sim 0.4$ and $\tau_{\text{s}} \sim 1.5$, to express its effects. Furthermore, we expect T_{e} to increase as the corona falls toward the BH, for the following two reasons. One is because, compared to the corona inside R_{in}, that the overlapping region must be more strongly cooled by the disk photons, and less efficiently heated by protons due to lower densities. The other is because, at about R_{cc}, the disk surface layer must evaporate into the corona, so it will take a fraction of a second (calculated at R_{cc}; Guilbert et al. 1982) for the evaporated electrons to be heated by protons via Coulomb interaction. Then, the observed $T_{\text{e}} \sim 100$ keV should be considered as a radial average over the corona.

Under the configuration as assumed above, we further speculate that, for some unspecified reasons, the corona has a number of "holes" (at least in the overlapping region between the disk and corona), through which the disk is directly visible (subsection 5.2). With these, the spectral composition of Cyg X-1 (and of GRO J1655−40) can be explained at least semi-quantitatively. Furthermore, this scenario can explain why the directly visible disk and the Fe-K lines of GRO J1655−40 are weaker than those of Cyg X-1 beyond what is expected by the inclination difference, because the holes would act as a vertical collimator to direct these disk-related emission components toward pole-on directions. The disk reflection would also be affected, but their intrinsically broad shape would remain rather intact.

In order to explain the fast variability, we may assume that the opening fraction of the coronal holes vary with time, due to some fluctuations in the disk evaporation rate. As the hole area diminishes by increased evaporation, we expect L_{seed} to increase and L_{raw} to decrease, as observed in the changes from LP to HP. Since the incremented portion of the corona must initially have a lower electron temperature due to the finite ion vs. electron coupling time, the HP spectrum is expected to be less Comptonized than in LP, again as observed. Electrons in that portion of the corona will be gradually heated up, on time scales of a fraction of a second, as they fall inwards across $R_{\text{in}}^{\text{tot}}$. This will explain, at least qualitatively, the XIS to PIN phase lag which would be too large to be explained by time-of-flight delays of photons in the Compton process.

6. Summary

Through the detailed analysis of the Suzaku data of Cyg X-1, we have obtained the following firm results:

1. The 0.7–400 keV Suzaku spectra are reproduced by the sum of a cool disk emission, two Compton continua both with reflection [$\Omega/(2\pi) \sim 0.4$], and a mildly broad Fe-K line.
2. The two Compton continua, with $\tau \sim 0.4$ and ~ 1.5, can be described by a common temperature of $T_{\text{e}} \sim 100$ keV, although the data do not exclude them having different temperatures.
3. The disk is characterized by $T_{\text{in}} \sim 0.2$ keV and $R_{\text{in}} \gtrsim 330$ km ($\gtrsim 15\ R_{\text{g}}$). Roughly half the disk emission gets Comptonized, while the rest forms the spectral soft excess.
4. When Cyg X-1 brightens up on a time scale of 1–200 s, a larger fraction of disk photons becomes Comptonized, although the disk parameters remain unchanged. The spectrum softens, as a result of a decrease in either T_{e} or τ.
5. A comparison between Cyg X-1 (with $i \sim 45°$) and GRO J1655−40 (with $i \sim 70°$) supports the view that the disk has a flat geometry and the Compton cloud is more spherical.

Combining these results with some theoretical considerations, we propose the following speculative scenario on the LHS of Cyg X-1 (and possibly of other BHBs). That is, the Componizing corona, with a roughly spherical (or thick torus) geometry, extends up to, say, $\sim 100\ R_{\text{g}}$, and the cool disk protrudes half way into it. The corona is highly inhomogeneous (as required by the double Compton τ), and has openings (as required by the soft excess) to allow a direct view of part of the disk. The hard X-ray intensity increases when the opening area of the corona decreases, and hence a larger number of disk photons become Comptonized.

References

Abubekerov, M. K., Antokhina, E. A., & Cherepashchuk, A. M. 2004, Astron. Rep., 48, 550

Bałucińska, M., & Hasinger, G. 1991, A&A, 241, 439

Basko, M. M. 1978, ApJ, 223, 268

Belloni, T., & Hasinger, G. 1990, A&A, 227, L33

Bregman, J., Butler, D., Kemper, E., Koski, A., Kraft, R. P., & Stone, R. P. S. 1973, ApJ, 185, L117

Di Salvo, T., Done, C., Życki, P. T., Burderi, L., & Robba, N. R. 2001, ApJ, 547, 1024

Done, C., Gierliński, M., & Kubota, A. 2007, ARA&A, 15, 1

Done, C., Mulchaey, J. S., Mushotzky, R. F., & Arnaud, K. A. 1992, ApJ, 395, 275

Done, C., & Życki, P. T. 1999, MNRAS, 305, 457

Dotani, T., et al. 1997, ApJ, 485, L87

Dove, J. B., Wilms, J., Nowak, M. A., Vaughan, B. A., & Begelman, M. C. 1998, ApJ, 298, 729

Ebisawa, K., et al. 1994, PASJ, 46, 375

Ebisawa, K., Ueda, Y., Inoue, H., Tanaka, Y., & White, N. E. 1996, ApJ, 467, 419

Esin, A. A., Narayan, R., Cui, W., Grove, J. E., & Zhang S.-N. 1998, ApJ, 505, 854

Fabian, A. C., Rees, M. J., Stella, L., & White, N. E. 1989, MNRAS, 238, 729

Feng, Y. X., Li, T. P., & Chen, L. 1999, ApJ, 514, 373

Frontera, F., et al. 2001a, ApJ, 546, 1027

Frontera, F., et al. 2001b, ApJ, 561, 1006

Gelino, D. M., Balman, Ş., Kiziloğlu, Ü., Yilmaz, A., Kalemci, E., & Tomsick, J. A. 2006, ApJ, 642, 438

Gierliński, M., Zdziarski, A. A., Done, C., Johnson, W. N., Ebisawa, K., Ueda, Y., Haardt, F., & Phlips, B. F. 1997, MNRAS, 288, 958

Gilfanov, M., Churazov, E., & Revnivtsev, M. 1999, A&A, 352, 182

Gilfanov, M., Churazov, E., & Revnivtsev, M. 2000, MNRAS, 316, 923

Greene, J., Bailyn, C. D., & Orosz, J. A. 2001, ApJ, 554, 1290

Guilbert, P. W., Fabian, A. C., & Stepney, S. 1982, MNRAS, 199, 19p

Hua, X.-M., Kazanas, D., & Titarchuk, L. 1997, ApJ, 482, L57

Ibragimov, A., Poutanen, J., Gilfanov, M., Zdziarski, A. A., & Shrader, C. R. 2005, MNRAS, 362, 1435

Ichimaru, S. 1977, ApJ, 214, 840

Inoue, H. 1989, in Proc. 23rd ESLAB Symp. on Two Topics in X-ray Astronomy, vol. 2 (Noordwijk: ESA), 783

Kanbach, G., Straubmeier, C., Spruit, H. C., & Belloni, T. 2001, Nature, 414, 180

Kazanas, D., Hua, X.-M., & Titarchuk, L. 1997, ApJ, 480, 735

Kitamoto, S., Takahashi, K., Yamashita, K., Tanaka, Y., & Nagase, F. 1990, PASJ, 42, 85

Kokubun, M., et al. 2007, PASJ, 59, S53

Koyama, K., et al. 2007, PASJ, 59, S23

Kubota, A., & Done, C. 2004, MNRAS, 353, 980

Kubota, A., & Makishima, K. 2004, ApJ, 601, 428

Kubota, A., Makishima, K., & Ebisawa, K. 2001, ApJ, 560, L147

Kubota, A., Tanaka, Y., Makishima, K., Ueda, Y., Dotani, T., Inoue, H., & Yamaoka, K. 1998, PASJ, 50, 667

Liang, E. P., & Nolan, P. L. 1984, Space Sci. Rev., 38, 353

Lightman, A. P., & White, T. R. 1988, ApJ, 335, 57

Lightman, A. P., & Zdziarski, A. A. 1987, ApJ, 319, 643

Liu, B. F., Mineshige, S., & Shibata, K. 2002, ApJ, 572, L173

Maccarone, T. J., Coppi, P. S., & Poutanen, J. 2000, ApJ, 537, L107

Magdziarz, P., & Zdziarski, A. A. 1995, MNRAS, 273, 837

Makishima, K., et al. 2000, ApJ, 535, 632

Makishima, K., Maejima, Y., Mitsuda, K., Bradt, H. V., Remillard, R. A., Tuohy, I. R., Hoshi, R., & Nakagawa, M. 1986, ApJ, 308, 635

Malzac, J., Beloborodov, A. M., & Poutanen, J. 2001, MNRAS, 326, 417

Margon, B., Bowyer, S., & Stone, R. P. S. 1973, ApJ, 185, L113

Marshall, F. E., Mushotzky, R. F., Petre, R., & Serlemitsos, P. J. 1993, ApJ, 419, 301

Miller, J. M. 2006, Astron. Nachr., 327, 997

Miller, J. M., Homan, J., & Miniutti, G. 2006b, ApJ, 652, L113

Miller, J. M., Homan, J., Steeghs, D., Rupen, M., Hunstead, R. W., Wijnands, R., Charles, P. A., & Fabian, A. C. 2006a, ApJ, 653, 525

Mitsuda, K., et al. 1984. PASJ, 36, 741

Mitsuda, K., et al. 2007, PASJ, 59, S1

Miyamoto, S., & Kitamoto, S. 1989, Nature, 342, 773

Miyamoto, S., Kitamoto, S., Iga, S., Negoro, H., & Terada, K. 1992, ApJ, 391, L21

Miyamoto, S., Kitamoto, S., Mitsuda, K., & Dotani, T. 1988, Nature, 336, 450

Morrison, R., & McCammon, D. 1983, ApJ, 270, 119

Mushotzky, R. F., Done, C., & Pounds, K. A. 1993, ARA&A, 31, 717

Narayan, R., & Yi, I. 1995, ApJ, 452, 710

Negoro, H., Miyamoto, S., & Kitamoto, S. 1994, ApJ, 423, L127

Nolan, P. L., et al. 1981, ApJ, 246, 494

Nowak, M. A., Vaughan, B. A., Wilms, J., Dove, J. B., & Begelman, M. C. 1999b, ApJ, 510, 874

Nowak, M. A., Wilms, J., Vaughan, B. A., Dove, J. B., & Begelman, M. C. 1999a, ApJ, 515, 726

Oda, M. 1977, Space Sci. Rev., 20, 757

Oda, M., Gorenstein, P., Gursky, H., Kellogg, E., Schreier, E., Tananbaum, H., & Giacconi, R. 1971, ApJ, 166, L1

Pottschmidt, K., et al. 2003, A&A, 407, 1039

Poutanen, J., & Svensson, R. 1996, ApJ, 470, 249

Remillard, R. A., & McClintock, J. E. 2006, ARA&A, 44, 49

Revnivtsev, M., Gilfanov, M., & Churazov, E. 1999, A&A, 347, L23

Revnivtsev, M., Gilfanov, M., & Churazov, E. 2000, A&A, 363, 1013

Revnivtsev, M., Gilfanov, M., & Churazov, E. 2001, A&A, 380, 520

Rykoff, E. S., Miller, J. M., Steeghs, D., & Torres, M. A. P. 2007, ApJ, 666, 1129

Serlemitsos, P. J., et al. 2007, PASJ, 59, S9

Shakura, N. I., & Sunyaev, R. A. 1973, A&A, 24, 337

Shapiro, S. L., Lightman, A. P., & Eardley, D. M. 1976, ApJ, 204, 187

Shimura, T., & Takahara, F. 1995, ApJ, 445, 780

Sunyaev, R. A., & Titarchuk, L. G. 1980, A&A, 86, 121

Sunyaev, R. A., & Trümper, J. 1979, Nature, 279, 506

Takahashi, T., et al. 2007, PASJ, 59, S35

Takahashi, H., et al. 2008, PASJ, 60, S69   (Paper I)

Takahashi, K., Inoue, H., & Dotani, T. 2001, PASJ, 53, 1171

Terada, Y., et al. 2008, PASJ, 60, S25

Watarai, K., Fukue, J., Takeuchi, M., & Mineshige, S. 2000, PASJ, 52, 133

Yamaoka, K., Uzawa, M., Arai, M., Yamazaki, T., & Yoshida, A. 2005, Chin. J. Astron. Astrophys. Suppl., 5, 273

Young, A. J., Fabian, A. C., Ross, R. R., & Tanaka, Y. 2001, MNRAS, 325, 1045

Zdziarski, A. A., & Gierliński, M. 2004, Prog. Theor. Phys. Suppl., 155, 99

Zdziarski, A. A., Gierliński, M., Mikołajewska, J., Wardziński, G., Smith, D. M., Alan Harmon, B., & Kitamoto, S. 2004, MNRAS, 351, 791

Zdziarski, A. A., Lubiński, P., & Smith, D. A. 1999, MNRAS, 303, L11

Zdziarski, A. A., Poutanen, J., Mikołajewska, J., Gierliński, M., Ebisawa, K., & Johnson, W. N. 1998, MNRAS, 301, 435